

**JOINT DOD/DOE PRS SIMULATOR UPGRADE:
LOAD PHYSICS STABILITY RISK
MITIGATION MANAGEMENT**

Dr Norman F. Roderick

Dr Robert E. Peterkin, Jr.

Dr Thomas W. Hussey

July 1997

Final Report

APPROVED FOR PUBLIC RELEASE; DISTRIBUTION IS UNLIMITED.

19971202 009

[DTIC QUALITY INSPECTED 8]



**PHILLIPS LABORATORY
Advanced Weapons and Survivability Directorate
AIR FORCE MATERIEL COMMAND
KIRTLAND AIR FORCE BASE, NM 87117-5776**

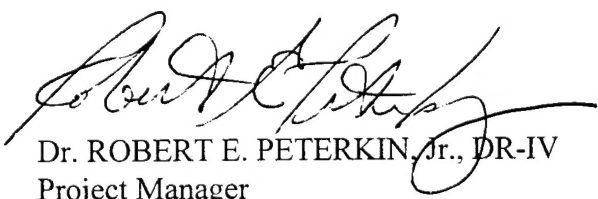
Using Government drawings, specifications, or other data included in this document for any purpose other than Government procurement does not in any way obligate the U.S. Government. The fact that the Government formulated or supplied the drawings, specifications, or other data, does not license the holder or any other person or corporation; or convey any rights or permission to manufacture, use, or sell any patented invention that may relate to them.

This report has been reviewed by the Public Affairs Office and is releasable to the National Technical Information Service (NTIS). At NTIS, it will be available to the general public, including foreign nationals.

If you change your address, wish to be removed from this mailing list, or your organization no longer employs the addressee, please notify PL/WSQ, 3550 Aberdeen Ave SE, Kirtland AFB, NM 87117-5776.

Do not return copies of this report unless contractual obligations or notice on a specific document requires its return.

This report has been approved for publication.



Dr. ROBERT E. PETERKIN, Jr., DR-IV
Project Manager



Dr. THOMAS W. HUSSEY, DR-IV
Chief, High Energy Sources Division

FOR THE COMMANDER,


WILLIAM G. HECKATHORN, Col, USAF
Director, Advanced Weapons
and Survivability Directorate

REPORT DOCUMENTATION PAGE			Form Approved OMB No. 0704-0188
<p>Public reporting burden for this collection of information is estimated to average 1 hour per response, including the time for reviewing instructions, searching existing data sources, gathering and maintaining the data needed, and completing and reviewing the collection of information. Send comments regarding this burden estimate or any other aspect of this collection of information, including suggestions for reducing this burden, to Washington Headquarters Services, Directorate for Information Operations and Reports, 1215 Jefferson Davis Highway, Suite 1204, Arlington, VA 22202-4302, and to the Office of Management and Budget, Paperwork Reduction Project (0704-0188), Washington, DC 20503.</p>			
1. AGENCY USE ONLY (Leave blank)	2. REPORT DATE	3. REPORT TYPE AND DATES COVERED	
	25 Jul 97	FINAL TECHNICAL REPORT, 20 Jun 94 - 31 Dec 94	
4. TITLE AND SUBTITLE JOINT DOD/DOE PRS SIMULATOR UPGRADE: LOAD PHYSICS STABILITY RISK MITIGATION MANAGEMENT		5. FUNDING NUMBERS PE: 000000 PR: DNA0 TA: AQ WU: 07	
6. AUTHOR(S) DR. NORMAN F. RODERICK DR. ROBERT E. PETERKIN, JR. DR. THOMAS W. HUSSEY		8. PERFORMING ORGANIZATION REPORT NUMBER PHILLIPS LABORATORY ADVANCED WEAPONS & SURVIVABILITY DIRECTORATE (WS) HIGH ENERGY SOURCES DIVISION (WSQ) PLASMA THEORY & COMPUTATION BRANCH (WSQA) 3550 ABERDEEN AVENUE S.E., KIRTLAND AFB, NM 87117-5776	
9. SPONSORING/MONITORING AGENCY NAME(S) AND ADDRESS(ES)		10. SPONSORING/MONITORING AGENCY REPORT NUMBER	
11. SUPPLEMENTARY NOTES			
12a. DISTRIBUTION AVAILABILITY STATEMENT APPROVED FOR PUBLIC RELEASE; DISTRIBUTION IS UNLIMITED.		12b. DISTRIBUTION CODE	
13. ABSTRACT (Maximum 200 words) Plasmas are subject to many instabilities that make control of their components particularly difficult. It is well known that z-pinches are subject to Rayleigh-Taylor-like instabilities. This report analyzes MJ-level, 50 ns gas-puff z-pinches performed on the Saturn accelerator at Sandia National Laboratory with the magnetohydrodynamic codes Mach2 and Mach3. This analysis indicates that the uniformity of the pinch depends on the thickness of the initial gas-puff. Three-dimensional calculations suggest that modes with azimuthal asymmetry cause only modest changes to the radiative yield of fast z-pinches.			
14. SUBJECT TERMS FAST Z-PINCHES, MAGNETOHYDRODYNAMIC CODES, PLASMA INSTABILITIES		15. NUMBER OF PAGES 52	
		16. PRICE CODE	
17. SECURITY CLASSIFICATION OF REPORT UNCLASSIFIED	18. SECURITY CLASSIFICATION OF THIS PAGE UNCLASSIFIED	19. SECURITY CLASSIFICATION OF ABSTRACT UNCLASSIFIED	20. LIMITATION OF ABSTRACT UL

CONTENTS

1. INTRODUCTION	1
2. Z-PINCH PHYSICS OVERVIEW.....	2
3. OVERVIEW OF MHD SIMULATIONS	3
4. TWO-DIMENSIONAL SIMULATIONS	4
4.1 TWO-DIMENSIONAL SIMULATIONS WITH GAS INJECTION.....	4
4.2 TWO-DIMENSIONAL SIMULATIONS FROM SPECIFIED INITIAL CONDITIONS.....	12
5. THREE DIMENSIONAL SIMULATIONS	13
6. CONCLUSIONS.....	16
6.1 CONCLUDE: TWO-DIMENSIONAL MHD SIMULATIONS WITH GAS INJECTION	16
6.2 CONCLUDE: TWO-DIMENSIONAL SIMULATIONS FROM SPECIFIED INITIAL CONDITIONS.....	17
6.3 CONCLUDE: THREE-DIMENSIONAL SIMULATIONS.....	17

Figures

Figure	Caption	Page
	Figure 1. Numerical representation of Saturn voltage waveform.	22
	Figure 2. Isodensity contours at $t = 0$.	
	(a) Annular gas injection	23
	(b) Cylindrical gas injection	24
	Figure 3. Density vs. radius at top electrode at $t = 0$.	
	(a) Annular gas injection	25
	(b) Cylindrical gas injection	26
	Figure 4. Isodensity contours at $t = 70$ ns.	
	(a) Annular gas injection	27
	(b) Cylindrical gas injection	28
	Figure 5. Isodensity contours at $t = 80$ ns.	
	(a) Annular gas injection	29
	(b) Cylindrical gas injection	30
	Figure 6. Isodensity contours.	
	(a) Annular gas injection at $t = 85$ ns	31
	(b) Cylindrical gas injection at $t = 88$ ns	32
	Figure 7. Fourier spectrum of mass-density at outer nozzle radius at $t = 0$.	
	(a) Annular gas injection	33
	(b) Cylindrical gas injection	34
	Figure 8. Fourier spectra of average mass-density for annular injection at $t = 70$ ns and $t = 80$ ns.	35
	Figure 9. Fourier spectra of average mass-density for cylindrical injection at $t = 70$ ns and $t = 80$ ns.	36
	Figure 10. Fourier spectra of average mass-density for annular injection and cylindrical injection when plasma sheath is at approximately 1.25 cm radius.	37
	Figure 11. Fourier spectra of average mass-density for annular injection and cylindrical injection when plasma sheath is at approximately 0.50 cm radius.	38

Figure 12. Mass isodensity plot, 8 cut planes and isodensity surface, at $t = 50$ ns for $\pm 50\%$ perturbation.	39
Figure 13. Mass isodensity plots for the $k = 2$ (top) and $k = 4$ (bottom) cut planes at $t = 62.5$ ns for the $\pm 5\%$ random density perturbation.	40
Figure 14. Mass isodensity plot near pinch $t = 62.5$ ns. (a) 16 cut planes (b) 16 cut planes and isodensity surface	41 42
Figure 15. Mass isodensity plots at pinch $t = 67.5$ ns. (a) 16 cut planes and isodensity surface (b) Outer isodensity surface	43 44
Figure 16. Radiated power vs. time for two-dimensional (solid line) and three- dimensional (dotted line) simulations with $\pm 5\%$ random density perturbations.	45

1. INTRODUCTION

The Defense Special Weapons Agency (DSWA, formerly the Defense Nuclear Agency) provides the ionizing radiation test capability for the Department of Defense, the individual services, and other Government agencies. These testing capabilities are used to ensure the ability of military systems to withstand the ionizing radiation inherent in the space environment and produced by nuclear weapons effects in space and the atmosphere. Over the past twenty years, the DSWA has developed simulator technologies and has acquired, maintained, and upgraded required simulators to satisfy evolving user test requirements for radiation environments. To address the technology required for the PRS simulator upgrade program, a cooperative program between DSWA and Sandia National Laboratories (SNL) has been organized. The objective of this program is to provide the necessary simulator upgrades for production x-ray testing in the cold to warm (1-15 keV) x-ray regime to meet other Government agency test requirements. This required total capability has become even more essential with the cessation of underground nuclear testing.

Initial planning and engineering studies were completed by the Joint Design Options Study Team (JDOST), a group of Government and industry pulsed power experts chartered by the program managers to formulate planning options for simulator upgrade development. JDOST recommended a risk mitigation effort to answer key questions concerning the critical design and engineering criteria to build an advanced PRS simulator within cost and schedule constraints. The risk mitigation effort targets specific technical areas for technology demonstrations that will help to ensure the PRS simulator upgrade program will meet the criteria set for performance, cost, and schedule.

The technical areas the risk mitigation program addressed are: the pulsed power drivers, power flow, prime power, testing technologies, and load physics. The results of efforts in each technical area will be integrated with the others to assure that program level risk is reduced to an acceptable level.

The present report addresses technical issues for the PRS simulator upgrade load physics portion of the risk mitigation effort. The objective of this effort is to apply the computational physics resources of the Phillips Laboratory's Advanced Weapons and Survivability Directorate to advance the understanding of how Raleigh-Taylor instabilities are born, grow, and mitigated in a z-pinch plasma. The specific focus of this effort is Raleigh-Taylor instability model development, assessment of the model's predictive capability on z-pinches produced by the Saturn pulsed power generator at Sandia National Laboratory-Albuquerque, and scoping the three-dimensional effects of plasma asymmetries during implosion.

2. Z-PINCH PHYSICS OVERVIEW

Imploding gas puff z-pinches are one method used to produce intense high energy density plasma sources for thermal and non-thermal x-ray production.^{1,2,3,4,5,6,7,8} In these implosions an annular or cylindrical preionized plasma is accelerated by the $\vec{J} \times \vec{B}$ Lorentz force produced by the currents flowing in the plasma toward the axis where stagnation and radiation production occurs. The hydromagnetic Rayleigh-Taylor instability is a well known source of nonuniform behavior in the electromagnetic implosion of such plasmas.^{9,10,11,12,13,14,15,16,17,18,19,20,21,22,23} This instability and the zipper effect due to nonuniform gas distribution in gas puff implosions can produce decreased radiation yields and increased radiation times in plasma implosions²⁴ compared to what is expected from simple one-dimensional analysis. Understanding the implosion and pinch dynamics is critical for optimizing and scaling load designs to obtain desired plasma and radiation performance levels. In this report we describe magnetohydrodynamic (MHD) simulations of a class of annular and cylindrical fill gas puff implosions in krypton driven by the Saturn pulsed power generator at Sandia.

Saturn has been used to drive a variety of imploding plasma loads. It delivers currents up to 10 MA with a characteristic rise time of 50 ns producing peak electrical powers of 15 TW.⁷ For pinch masses studied here the Saturn generator produced implosions with final velocities of over 100 cm / μ s for both annular and cylindrical fill

gas injections.²⁵ In addition to the high final velocities the uniform fill experiments produced pinches which appeared to be more uniform than the annular gas injection initial conditions.

In Section 3, we give a brief overview of the MHD codes used to study the Saturn z-pinch experiments. In Sections 4 and 5, we discuss the particular simulations performed in two and three spatial dimensions respectively. In Section 4, we obtain an understanding of the experimental observation that the pinches from initially cylindrical gas filled experiments appear to be more uniform than pinches from initially annular gas filled experiments. In Section 5, we discuss the differences in the radiative yield between 2- and 3-dimensional simulations of similar initial states. Our conclusions are given in Section 6.

3. OVERVIEW OF MHD SIMULATIONS

Simulations were carried out in two and three dimensions to study the dynamics of the plasma implosion and the development and evolution of the hydromagnetic Rayleigh-Taylor instability. The majority of the work on this task concentrated on two-dimensional simulations with a small effort looking at three dimensional behavior of the instability. The two-dimensional simulations were carried out using Mach2,²⁶ and the three-dimensional simulations were done with Mach3.²⁷ The Mach software, Mach2 and Mach3, are time dependent Arbitrary Lagrangian Eulerian (ALE) simulation codes that solve the resistive MHD continuity, momentum, energy, and magnetic field equations on a computational grid composed of hexahedral cells. The codes use finite volume differencing. They are single fluid three temperature (electron, ion, and radiation) codes that use either analytic models or tabular values (SESAME tables²⁸ at Los Alamos National Laboratory) for the state and transport variables. In modeling the dynamics during the implosion, when the plasma is optically thin, a simple radiation emission model employing non-LTE opacities^{29,30} is used. This radiation model works quite well during the implosion when the plasma is optically thin, but is not expected to give accurate quantitative results for the radiation pulse at stagnation.

4. TWO-DIMENSIONAL SIMULATIONS

Mach2 is a 2 and $\frac{1}{2}$ dimensional code that solve the MHD equations on a two-dimensional grid but in general carries all three components of the velocity and magnetic fields. In addition to the features mentioned above common to Mach2 and Mach3, Mach2 has a generalized Ohm's law that includes the Hall effect and thermally generated magnetic field terms and can be run with a strength of materials option. Neither of these features were used in the simulations reported here.

In the 2 and $\frac{1}{2}$ dimensional simulations, the Saturn generator was modeled with a single-loop equivalent R-L circuit driven by the voltage waveform shown in Figure 1. For these simulations the series resistance was 1/6 ohm and the inductance 10 nH. The experimental anode-cathode gap was 2.0 cm, and unless otherwise stated this value was used in the numerical calculations.

In Section 4.1 we discuss implosion calculations that were performed on initial mass density distributions computed from separate gas injection calculations (also done with Mach2) to obtain physically-reasonable initial conditions. In Section 4.2 we discuss calculations that used simple applied initial conditions that only approximately correspond to the state that develops from the gas injection calculations. These later calculations are done to guide the 3-D calculations discussed in Section 5.

4.1 Two-Dimensional Simulations with Gas Injection

The first two-dimensional simulations started with a calculation of the gas injection into the implosion diode and follow the implosion dynamics to pinch. Calculations have been made for both the annular fill (annular nozzle) and the cylindrical fill (conventional nozzle) experiments. For both cases the initial conditions for the calculation were obtained from a gas injection calculation also made using Mach2. The injection calculations were started in the diode geometry to be used for the implosion calculations. Gas was injected, using ideal nozzle exit conditions³¹ by specifying the velocity and temperature at the nozzle exit, across the cathode surface at the location of the nozzle in the experiment. Injection velocity, mass-density, and temperature were

chosen to be those associated with the design Mach numbers of the experimental nozzles. The injected gas for each nozzle was krypton. The annular nozzle had a 4.5 cm outer diameter, a 2.5 cm inner diameter, a nozzle angle of 5° inward, and was designed for Mach 8. The cylindrical fill nozzle had a 4.5 cm diameter, a nozzle angle of 0° , and was designed for Mach 6. The anode boundary condition allowed hydrodynamic flow to pass through the plane of the anode simulating the wire anode used in the experiment. For the simulations reported here, the injection calculations were run until the gas distribution in the diode reached steady state for each nozzle configuration. At this time the injected gas from both type nozzles shows an expansion fan at the outer nozzle radius characteristic of gas expansion from a nozzle into a region at lower pressure than the gas pressure at the exit (underexpanded nozzle)³¹. The expansion fan gives the outer regions of the gas a r-z distribution of mass-density. Additionally there is an expansion fan at the inner edge of the annular nozzle producing an r-z mass-density distribution going inward toward the axis. The mass isodensity contours at steady state for both types of nozzle are shown in Figure 2. Figure 3 shows plots of mass-density versus radius at 2.0 cm axial distance from the nozzle exit for both nozzles at steady state. The annular injection shows the inward 5° injection angle and both inner and outer expansion fans. The mass-density profile is two-dimensional over all of its radial extent. For the uniform injection process at injection, the center of the gas injection region has a flat top over a wide region with the mass-density decreasing rapidly in the wings of the expansion fan. The total masses inferred from the experimentally-measured implosion time applied to a slug model driven by the Saturn voltage waveform were $300 \mu\text{g}$ for the annular fill and $500 \mu\text{g}$ for the cylindrical fill. The injection mass-density was adjusted to give these experimentally inferred masses. For the annular nozzle case this gave a mass-density in the center of the nozzle region of $1.5 \times 10^{-2} \text{ kg/m}^3$, and for the uniform-fill case a center line mass-density of $1.57 \times 10^{-2} \text{ kg/m}^3$.

The two-dimensional implosion calculations were initiated from these mass-density conditions with a plasma temperature chosen to give an average ionization

fraction of approximately 0.5, consistent with the average ionization fraction obtained from the ultraviolet flashboard used in the experiment. Using the Saturn voltage waveform and simple single-loop lumped circuit model for the generator described previously, the overall computational results for both cases are in agreement with the experimental data. Current peaks for the experiment and computation were a nominal 10 MA. The implosion time for the experiment was measured by taking the slope of the maximum current rise and extrapolating it to the time base to get a start time, and using the time at which the radiated signal measured by XRD's reached 10% of its peak. Note this is not the same as the time measured from the beginning of the voltage pulse which is the time we will be using soon in discussing the details of the simulations. This method gives an implosion time for the annular gas fill experiment of 53 ns. Using a similar technique for the start time in the calculations but using 10% of the radiated power from the calculations gives an implosion time of 51 ns. For the cylindrical fill, which is of larger mass, the experimental implosion time is 56 ns and the computational implosion time is 55 ns.

Now we will consider some details of the implosions for both the annular and cylindrical injection cases. We now measure time from the beginning of the voltage pulse. Throughout much of the implosion, the behavior of the plasma is similar for both cases. Figures 4, 5, and 6 show mass isodensity contour plots for the annular and uniform injection cases. These figures show the two plasma implosions when they are at approximately the same radial location. There are timing differences due to the mass difference between the annular initial condition ($300\mu\text{g}$), and the cylindrical fill initial conditions ($500\mu\text{g}$). The differences in gas injection angle combined with the mass difference produce some spatial variations as well. In both calculations the magnetic field initially penetrates into the plasma and a current sheath a few millimeters thick develops at the plasma vacuum interface. This sheath thickness is characteristic of the relatively cold, low-conductivity krypton plasma initiated by the flashboards. As the current rises the plasma heats and the field penetration distance is reduced due to the higher conductivity of the hotter plasma. The current continues to rise and the magnetic

pressure eventually begins to act as a magnetic piston to accelerate the dense plasma toward the axis. At the early stages of this process a relatively small amount of magnetic flux diffuses into the plasma ahead of the magnetic piston. The main portion of the plasma starts to move noticeably at approximately 44 ns into the voltage pulse for the cylindrical injection case and at approximately 45 ns for the annular injection case. At these times the field has had time to diffuse approximately 5 millimeters into high-density region of the plasma column for both cases. As the generator current rises the piston speed increases and a shock forms as the piston motion becomes supersonic with respect to the injected plasma in front of it. The shock formed by the piston overtakes the field that had diffused ahead at approximately 65 ns for the annular injection calculation and at approximately 69 ns from the uniform injection calculation. Past these times a shock wave / current sheath is formed ahead of the piston in both calculations. Because of the supersonic penetration of the shock wave / current sheath, the only region experiencing acceleration and thus subject to an instability similar in nature to the classical Rayleigh-Taylor instability is that between the shock and the piston. For the piston speeds and conductivities of this simulation, this is a thin region as shown in the mass-density contour plots at 70 ns. Figure 4. In these plots the instability can also be seen for both cases.

The instability itself starts in the portion of the plasma being accelerated at the plasma magnetic field interface. The origin of the instability is the two-dimensional nature of the expansion fan produced by the injection process. The r-z mass-density variation in the expansion fan is the seed for the instability. The axial mass-density profile through this region at constant radius can be represented by a Fourier series. This series contains an infinite number of terms and can be thought of as exciting an infinite number of modes in the plasma. In a finite numerical model the number of modes is limited by the number of zones present—48 cells per centimeter in both axial and radial directions for the calculations presented here. Figure 7 shows the absolute value of the Fourier transform (power spectral density) of the mass-density versus mode-number³² at approximately 2.27 cm radius just before the current is switched on for both the annular

and the uniform injection cases. This radial location is just outside the nozzle exit. Both cases show all the modes have small amplitudes. The long wavelength, low mode-number, modes have the largest amplitude, and the amplitudes decrease for the shorter wavelength, higher mode-number, modes. Fourier analysis of the mass-density using an average over the non-uniform region of the expansion fan shows similar power spectra.

The instabilities for both the annular and uniform-fill implosions initially develop in the same manner. The instability shows the classic bubble spike characteristics of the Rayleigh-Taylor instability. Bubbles of light fluid, here the magnetic field, rise into the heavy fluid, here the plasma; and spikes of plasma fall into the magnetic field. The bubble rise is accompanied by mass being removed from the bubble region and moved into the spikes. Both short wavelength and long wavelength modes are present and growing. The first modes observed in the contour plots have a short wavelength, approximately 0.8 mm for both cases. The early appearance of the short wavelength modes is consistent with linear theory where the growth is exponential and which shows the fastest growing modes have short wavelength. This evolution from short wavelength to longer wavelength is the same type of behavior seen computationally and experimentally in annular plasma implosions initiated from thin foils.²⁰ As the short wavelength modes saturate, longer wavelength modes which are present and continue to grow become more noticeable.

As the instability develops mass continues to flow into the unstable shock wave / current sheath region from the undisturbed plasma. The mass accretion replenishes some of the mass lost from the bubbles into the spikes. This process continues as the material in the gas puff is swept up and accelerated to smaller radius by the magnetic piston. The mass accretion process in the thick annular and cylindrical fill cases provides an effective “snowplow stabilization”^{33,34,35} for the early phases of gas-puff implosions. As long as mass is present ahead of the accelerating plasma, the unstable region continues to grow but in a non-exponential manner. This region is analogous to the penetration of the mixing layer into the heavy fluid in the conventional hydrodynamic Rayleigh-Taylor problem which starts as short wavelength exponential growth and evolves to a non-

exponential process.³⁶ An additional difference here is the Atwood number of 1 characteristic of the light fluid being a magnetic field produces a mixing region where the disturbances, while nonlinear do not show the turbulent nature of the classical mixing layer.

The gas-puff situation is initially somewhat different from plasma implosions initiated from thin foils or the two-dimensional models of wire implosions. For the foil and wire plasmas the plasma is formed from the initiation of a relatively thin solid by the high current supplied by the generator. For these cases the current flows in the entire plasma from the time of initiation, and the entire plasma region is accelerated. The result is that there is little or no mass available in front of the accelerated region to flow into the unstable regions. These thin annular implosions show the same structural evolution from short wavelength to longer wavelength as seen here, but in these thin cases while the short wavelengths saturate, longer wavelengths show continuing exponential growth as they run out of mass due to the thickness of the annulus.

The same situation occurs here for the annular puff, although at a later time due to the thickness of the initial annulus and the initial magnetic field configuration in the plasma. After the magnetic piston passes over the inner nozzle radius there is little mass to flow into the unstable shock wave / current regions. This occurs at approximately 75 ns for both cases. Figure 5 shows the mass-density contour plots for both the annular and uniform injection calculations at 80 ns at a time shortly after the accelerated plasma passes 1.25 cm, the location of the inner radius of the nozzle for the annular injection case. The reduced density near the upper electrode for the annular case results from mass flow out of the electrode region at the anode. Inside 1.25 cm radius, the cathode is again solid when there is an annular nozzle so mass cannot cross this surface inside this radial location. The nozzle for the cylindrical fill extends all to the axis. Therefore, the mass-density is reduced at both the upper and lower electrode as a result of mass flow out of the inter-electrode region into the nozzle on the lower electrode and through the open wire upper electrode. The characteristic wavelength in the region near the nozzle when the shock wave / current sheath at this time is now slightly less than 2 mm. For the

annular injection case, the sheath farther away from the nozzle is still accreting mass from the expansion fan in front of the inner nozzle radius. To this point the instability behavior is similar in both calculations.

Past this time for the annular case the entire plasma region becomes a thin shell accelerated by the magnetic piston similar to the foil implosion type plasmas. This process starts at the nozzle electrode and progresses upward across the plasma as the mass associated with the inner expansion fan is entirely swept up. With the end of the mass accretion, the modes begin to return to exponential growth due to mass loss from the bubbles. Figure 6 shows the mass-density contours for both cases at a radius of approximately 0.5 cm. This location is reached at 85 ns for the annular puff and at 88 ns for the cylindrical fill case due to the mass differences between the two cases. Both cases show a reduced density region near the upper electrode that is caused by flow out through the wire electrode. Additionally there is a reduced density region near the nozzle electrode for the cylindrical fill case where mass flows into the nozzle. At this radial location several bubbles in the annular implosion case have become quite large. These large bubbles are just beginning to rupture. For the cylindrical fill case at this time, the unstable region has a smaller radial extent, smaller bubbles, and the growth of the region remains non-exponential due to the continuing accretion of mass.

Just prior to pinch for the annular case, the characteristic wavelength of the modes which have returned to exponential growth is approximately 3 mm. The annular shell then bursts at the bubbles in several axial locations accelerating some low-density material to the axis ahead of the main part of the plasma shell. As this low-density material stagnates before the main body of the shell arrives, it produces regions of high-speed axial flow in excess of $100\text{cm} / \mu\text{s}$ along the axis. This is comparable to the final peak average radial implosion velocity of approximately $120\text{cm} / \mu\text{s}$. The piston continues to accelerate the denser portion of the shell producing a stagnation of the thickened more disk-like spike regions that remained after the bubbles burst. Stagnation for the annular case occurs first at the anode end of the diode in a 'zippering' manner since the low mass was mismatched for the nozzle. The combination of the separate spike

regions and the high-speed axial flow of the low-density material in the annular case produce a very non-uniform pinch region.

For this cylindrical fill case, however, the mass in front of the unstable region extends all the way to the axis. This mass prevents the return to exponential instability growth. The ‘mixing’ layer continues to thicken from both the instability and the radial convergence, but in a non-exponential manner. Just prior to pinch the characteristic wavelength for the uniform case is slightly larger than 2 mm (2/3 the size of the annular fill case). For the cylindrical case, the bubbles stagnate when the mode amplitude (bubble to spike distance) is approximately the shell radius. Peak axial velocities for this case were a few 10’s cm / μ s compared to the peak radial velocities of over 100cm / μ s. This results in a thinner shell at stagnation than the annular case and a more uniform pinch.

The instability evolution can also be seen in the Fourier spectra for the two cases. Figure 8 shows the Fourier amplitude of the average mass-density for the annular case and Figure 9 shows the Fourier amplitude for the uniform injection case at 70 ns and 80 ns. To obtain these spectra we first took a simple average of the radial mass-density distribution of the unstable region of the plasma for each axial strip of the calculation. We then took the Fourier transform of this axially-varying mass-density average. The spectra presented have been normalized to the average background mass-density and are plotted from mode-number 1 to mode-number 48. From this data we can see a growth in both long wavelength and short wavelength modes. However, the longer wavelength modes show more growth in both cases. At 70 ns the radial location for the annular case is before the implosion has passed over the inner radius of the nozzle. For both cases the normalized mode amplitudes are approximately equal at this time. By 80 ns the implosion of the annular fill—which is now inside the inner radius of the nozzle—is no longer accreting mass. At this time we see not only the evolution to longer wavelength, lower mode-number, mentioned previously, but also a significant difference in normalized spectra amplitudes. The annular case is at significantly larger amplitude than the uniform-fill implosion.

This can be seen by direct comparison between the annular and the cylindrical injection cases as shown in Figure 10 and Figure 11 where we have plotted the spectral amplitude at approximately the same spatial location for each case. Figure 10 shows the spectra when the plasma sheath has reached approximately 1.25 cm, the radial location of the inner radius of the annular nozzle, and the conditions shown in the Figure 5 contour plot. The time the implosion reaches this approximate radial location is 75 ns for both cases. Up to this time both cases have been accreting mass. This direct comparison shows amplitudes to differ only slightly. At a radial location of approximately 0.5 cm, the conditions shown in the Figure 6 contour plot, Figure 11 shows the spectral amplitudes have significantly different characteristics. The annular case clearly has higher amplitude, as would be expected from the contour plots. The growth is significantly higher at low mode-numbers, but there is continued growth at high mode-number. This increase at higher mode-numbers is attributed partly to the significant nonlinear behavior and more step-function like behavior of the mass-density profile that occurred as the bubbles distend and burst.

4.2 Two-Dimensional Simulations from Specified Initial Conditions

Since the gas injection process adds additional computational time to the simulation process, and since the three dimensional calculations were to be carried out on only a small region of the problem domain, a series of two-dimensional simulations were carried out to see if approximately the same instability growth and evolution could be attained starting from the simpler right circular cylinder initial conditions often used to study gas puff implosions. By approximately the same instability growth and evolution we mean the same type of wavelength cascade and save final wavelength and amplitudes of the most visible waves just prior to pinch. Calculations were made for right circular uniform fill cylinders of radius 2.25 cm and of right circular annuli of inner radius 1.25 cm and outer radius 2.25 cm. For these cases there is no physical seed to the instability. Therefore, a random density perturbation was used to initiate the growth. Calculations were carried out with random perturbation amplitudes 0, $\pm 1\%$, $\pm 5\%$ and $\pm 10\%$ applied to every cell. Results showed that the $\pm 5\%$ random density perturbation gave the closest

agreement with the gas injection calculations. The $\pm 1\%$ case gave approximately the same wavelength prior to stagnation but at too low an amplitude. The $\pm 10\%$ case gave amplitudes that were too large and wavelengths that were slightly too long. From this we conclude that a $\pm 5\%$ random density perturbation can be used to approximate the behavior of the more complete gas injection calculations to study the basic instability growth and evolution.

5. THREE DIMENSIONAL SIMULATIONS

The three-dimensional calculations were of an exploratory nature and done on a restricted problem domain compared to the two-dimensional simulations. Calculations were made to investigate three-dimensional effects for the uniform fill gas puff. Basic linear theory for the growth of the hydromagnetic Rayleigh-Taylor instability indicates that the growth in the $r - \theta$ plane should occur at growth rates roughly an order of magnitude lower than those in the $r-z$ plane, and that therefore the $r-z$ (two-dimensional) growth should dominate for perturbations started with equal amplitude.

The Mach3 simulations used a sine squared current waveform with a 55 ns quarter cycle and a 9.5 mega-ampere current maximum. This profile is similar to the current produced by the Saturn voltage waveform. These initial calculations were carried out for a restricted region of the problem identified from the characteristics of the two-dimensional simulations.

The first exploratory calculations carried out for this task involved looking at single mode three-dimensional growth. From the two-dimensional calculations of the cylindrical fill, the most unstable wavelength was found to be approximately 2 mm. This wavelength was used for the periodic $r-z$ plane mode. Additionally because there are 8 return current posts for these gas puff implosions the three-dimensional calculations were performed to look at what affect a eight fold symmetric perturbation would have on the instability. The $r - \theta$ plane mode was taken to be an $m=8$ periodic perturbation. These simulations used a $1/8^{\text{th}}$ segment of the 2π radians of the entire gas fill. The perturbation was chosen to be periodic in both $r-z$ and $r - \theta$ plane with an amplitude of $\pm 5\%$.

corresponding to the perturbation level that best represented the gas injection calculations and the experimental results.

The radiation model used throughout these calculations was the emission model using non-LTE opacities.^{29,30} While the model has limited use in terms of accurately predicting the radiated yield, we consider it to be reasonable for comparing differences in instability evolution between two-dimensional and three-dimensional calculations. The calculation showed mass flow from the bubbles to the spikes in both the $r-z$ and $r-\theta$ planes.

Despite the somewhat increased mass loss from the spike, the stagnation time and amplitude of the radiation pulse produced were essentially the same as for the two-dimensional case. The addition of a perturbation in the $r-\theta$ plane had no significant effect on the stagnation or the radiation pulse at this $\pm 5\%$ level single wavelength perturbation.

Next a full 2π geometry simulation was made using a large amplitude long wavelength perturbation in both the $r-z$ and $r-\theta$ planes. The calculation used 64 cells in the radial direction to the edge of the plasma (2.25 cm), 64 cells in the axial direction between the electrodes (1.60 cm), and 32 cell in the azimuthal direction. The $r-z$ plane perturbation had a wavelength of 0.8 cm and amplitude of $\pm 50\%$, larger than anticipated in experimental conditions. The $r-\theta$ plane had an $m=4$ perturbation also of $\pm 50\%$ amplitude. This level of perturbation had a significant effect on the pinch characteristics. Figure 12 shows the mass density for this simulation prior to pinch at 50 ns when the instability is well into the nonlinear regime of growth.. The figure shows 8 planes cut through the plasma density and an isodensity surface for density above $0.3 \text{ kg} / \text{m}^3$ for all cells in the problem. The classical Rayleigh-Taylor spike and bubble structure are easily recognized in both the $r-z$ and $r-\theta$ planes. The large amplitude effects in both the $r-z$ and $r-\theta$ planes are evident. For this large amplitude perturbation the strong azimuthal variations are an indication of important three-dimensional effects.

The final simulation discussed here is a full geometry simulation with features characteristic of those in the Saturn high velocity implosions. Here a 5% random density perturbation was applied to each cell in both the $r-z$ and $r-\theta$ planes. The calculation also used 64 cells in the radial direction to the edge of the plasma (2.25 cm), 64 cells in the axial direction between the electrodes (2.00 cm), and 32 cell in the azimuthal direction. Figures 13 and 14 show the mass-density at 62.5 nanoseconds slightly before the plasma assembles on axis (pinch). The initial perturbation level is small, a 5% random perturbation on the uniform background density in every cell in each direction. Figure 13 shows slice planes cutting vertically through the plasma column starting at the axis ($r=0$) and going to the original plasma location ($r=2.25$ cm). The slices are taken at two azimuthal locations ($k = 2$ and $k = 4$ azimuthal planes). Any three dimensional features show as differences between these two slice planes. From these it is clear that the perturbations in the $r-z$ plane are significant, but that three dimensional effects are small. This is consistent with linear stability theory and two-dimensional calculations. Figure 14 shows two three-dimensional representations of the plasma implosion at this time viewed from an angle of approximately 45° to the pinch axis (looking down at the plasma). Figure 14a shows 16 slices made vertically through the plasma (every other cell in the azimuthal direction). Figure 14b shows this representation again but now with an isodensity surface enclosing density above $0.3\text{kg} / \text{m}^3$ included for all cells in the problem. Again we can see the three dimensional effects are small. Figure 15 show mass-density during pinch ($t = 67.5$ ns) viewed from an angle of approximately 135° to the pinch axis (looking up at the pinch).. Figure 15a shows 16 slices made vertically through the plasma (every other cell in the azimuthal direction) and an isodensity enclosing density above $0.2\text{kg} / \text{m}^3$ for all cells. Figure 15b shows the isodensity surface enclosing density above $0.01\text{kg} / \text{m}^3$, all of the mass in the implosion, for all cells in the problem. These figures show the plasma now has some three dimensional (possibly helical) structure. The $r-z$ (two-dimensional effects) are dominant however. The three-dimensional effects even at pinch are small. Figure 16 shows radiated power vs. time for

this case along with the radiated power for a two-dimensional simulation. There is essentially no difference in the peak radiated power and general pulse shape despite the fact that some three-dimensional features are present in the mass-density distribution. From this we conclude that small three dimensional effects do not significantly affect the pulse time or radiated power.

6. CONCLUSIONS

6.1 Conclude: Two-Dimensional MHD Simulations with Gas Injection

We have performed two-dimensional magnetohydrodynamic simulations of gas-puff implosions driven to velocities over $100\text{cm} / \mu\text{s}$ by the Saturn pulsed power generator. The calculations were carried out from an initial vacuum diode into which krypton gas was injected from both annular and circular (uniform-fill) nozzles. The implosions were driven by a numerical circuit and voltage waveform characteristic of the Saturn generator. Implosion times and velocities were in good agreement with experiments. Mass average radial velocities prior to stagnation were in excess of $100\text{cm} / \mu\text{sec}$ for both types of gas injection schemes. Both injection cases experienced the hydromagnetic Rayleigh-Taylor instability. The instability started from the nonuniform axial mass-density distribution, which always occurs for nozzles expanding into vacuum or low-pressure regions. The instability, observed both in contour plots and Fourier analysis, evolved with short wavelengths appearing first and with longer wavelengths becoming dominant as the implosion progressed.

The initial nonlinear stages were characterized by the propagation of a shock wave/current sheath containing the unstable region into the undisturbed region of the injected plasma. This propagation becomes supersonic with respect to the undisturbed plasma. During this phase the unstable region continued to accrete mass from the initially undisturbed plasma in front of it, and resembled a classical hydrodynamic Rayleigh-Taylor mixing layer. The wavelength and amplitude of the instability were similar in both cases. The evolution of the cylindrical injection case proceeded in this

manner until stagnation when the mixing layer like region reached the axis. The annular injection case displayed a different behavior after the unstable region stopped accreting mass after passing over the inner radius of the injection nozzle. After mass accretion stopped, the annular implosion growth increased significantly and the instability bubbles burst in a manner similar to that seen in thin foil and multiple wire array implosions. This disruption of the plasma shell resulted in greater average thickness, a more disk like structure, and high-speed flows on axis. These conditions produced a more nonuniform pinch for the annular injection case than for the cylindrical injection case in the simulations, and this is consistent with experimental behavior.

6.2 Conclude: Two-Dimensional Simulations from Specified Initial Conditions

Two-dimensional simulations can be started from a simple right circular cylinder or right circular annulus with a random density perturbation to reproduce the instability characteristics of the implosion of an initial state without a random perturbation that is a consequence of a gas injection calculation. For the high speed krypton gas-puff implosions studied here an initial density perturbation of $\pm 5\%$ was appropriate to reproduce the gas injection instability characteristics seen in the simulations and in experiment.

6.3 Conclude: Three-Dimensional Simulations

A limited number of exploratory simulations were carried out with Mach3 and to begin the study of three-dimensional effects in z-pinch implosions. From these limited number of simulations no general conclusions can be made on the general area of three-dimensional effects. Some limited conclusions can be drawn form the simulations that were completed. A small amplitude ($\pm 5\%$) single mode ($m=8$) excitation in the $r - \theta$ plane for the most unstable wavelength in the r - z plane (also initialized with a $\pm 5\%$ random amplitude) shows some added growth as mass moves form the bubble to spikes in both the r - z and $r - \theta$ planes. The growth is dominated by the r - z plane behavior and

while some small effects were visible it did not modify the implosion time or radiation pulse from results seen in equivalent the two-dimensional simulations. This is consistent with linear theory which indicates reduced growth in the $r - \theta$ plane. Full 2π geometry simulations at large amplitude, $\pm 50\%$ periodic perturbations in the r - z (0.8cm wavelength) and $r - \theta$ ($m=4$) planes, showed significant effects could be produced at amplitudes significantly above those expected in experiment. Simulations were also made at small amplitude, $\pm 5\%$ random perturbations in both the r - z and $r - \theta$ planes, for the full experimental geometry. These conditions are closer to those expected experimentally. These produced slight visible differences in the density distribution, but the instability was again dominated by the r - z plane growth. Implosion time and radiation pulse were again essentially the same as the two-dimensional results. From these simulations we can tentatively conclude that small amplitude perturbations in the $r - \theta$ plane do not significantly influence the implosions.

REFERENCES

¹ J. Shiloh, A. Fisher, and N. Rostoker, Phys. Rev. Lett. **40**, 515 (1978).

² J.H. Degan, R.E. Reinovsky , D.L. Honea, R.D. Bengston, J. Appl. Phys. **52**, 6550 (1981).

³ W. Clark, R. Richardson, J. Brannon, M. Wilkinson, and J. Katzenstein, J. Appl. Phys. **53**, 5552 (1982).

⁴ R.E. Mars, D.D. Dietrich, R.J. Fortner, M.A. Levine, D.F. Price, R.E. Stewart, and B.K.F. Young, Appl. Phys. Lett. **42**, 946 (1983).

⁵ B.A. Hammel and L.A. Jones. Appl. Phys. Lett. **44**, 667 (1984).

⁶ R.B. Spielman, D.L. Hanson, M.A. Palmer, M.K. Matzen, T.W. Hussey, and J.M. Peek, J. Appl. Phys. **57**, 883 (1985).

⁷ D.D. Bloomquist, R.M. Stinnett, D.H. McDaniel, J.R. Lee, A.W. Sharpe, J.A. Halbleib, L.G. Shlitt, P.W. Spence, and P. Corcoran, *Proceedings of the 6th Institute of Electrical and Electronic Engineers Pulsed Power Conference*, Arlington, VA, edited by P.J. Turchi and B.H. Bernstein. Institute of Electrical and Electronic Engineers, New York, 1987), p. 310.

⁸ M.K. Matzen, Phys. Plasmas. **4** 1519 (1997).

⁹ F.L. Curzon, A. Folkierski, R. Latham, and J.A. Nation, Proc. Royal Soc. A **257**, 386 (1960).

¹⁰ E.G. Harris, Phys. Fluids **5**, 1057 (1962).

¹¹ N.F. Roderick, T.W. Hussey, R.J. Faehl, and R.W. Boyd, Appl. Phys. Lett. **32**, 273 (1980).

¹² T.W. Hussey, N.F. Roderick, and D.A. Kloc, J.Appl. Phys. **51**, 1452 (1980).

¹³ R.E. Reinovsky, D.L. Smith, W.L. Baker, J.H. Degnan, R.P. Henderson, R.J. Kohn, D.A. Kloc, and N.F. Roderick, IEEE Trans. Plasma Sci. **PS-10**, 73 (1982).

¹⁴ N.F. Roderick, B.J. Kohn, W.F. McCullough, C.W. Beason, J.A. Lupo, J.D. Leterio, D.A. Kloc, and T.W. Hussey, Laser Part. Beams **1**, 181 (1983).

¹⁵ B.J. Kohn, N.F. Roderick, and C.W. Beason, J. Appl. Phys. **54**, 4348 (1983).

¹⁶ A.B. Budko, F.S. Felber , A.I. Kleev, M.A. Liberman, and A.L. Velikovich, Phys. Fluids B **3**, 598 (1989).

¹⁷ A.B. Budko, M.A. Liberman, A.L. Velokovich, and F.S. Felber, Phys. Fluids B **2**, 1159 (1990).

¹⁸ C. Deeney, P.D. LePell, F.L. Cochran, M.C. Coulter, K.G. Whitney, and J. Davis, Phys. Fluids B **5**, 992 (1992).

¹⁹ F.L. Cochran, J. Davis, and A.L. Velikovich, Phys. Plasmas **2**, 2765 (1995).

²⁰ Peterson, R.L. Bowers, J.H. Brownell, A.E. Greene, K.D. McLenithan, T.A. Oliphant, N.F. Roderick, and A.J. Scannapieco, Phys. Plasmas **3**, 388 (1996).

²¹ J.H. Hammer, J.L. Eddleman, P.T. Springer, M. Tabak, A. Toor, K.L. Wong, G. Zimmerman, C. Deeney, R. Humphreys, T.J. Nash, T.W.L. Sanford, R.B. Spielman, and J.S. DeGroot, Phys. Plasmas **3**, 2063 (1996).

²² J.S. DeGroot, A. Toor, S.M. Golberg, and M.A. Liberman, Phys. Plasmas **4**, 737 (1997).

²³ M.R. Douglas, C. Deeney, and N.F. Roderick, Phys. Rev. Lett., **78**, 4577 (1997).

²⁴ T.W. Hussey, M.K. Matzen, and N.F. Roderick, J. Appl. Phys. **59**, 2677 (1986).

²⁵ R.B. Spielman, T.L. Gilliland, R. Humphreys, D. Jobe, J.S. McGurn, T.J. Nash, J.L. Porter, L.E. Ruggles, and J. Seamen, IEEE Conference Record-Abstracts, 1994 IEEE International Conference on Plasma Science, 94CH3465-2 (Institute of Electrical and Electronic Engineers, Piscataway, New Jersey, 1994), p. 161.

²⁶ R.E. Peterkin Jr., J.H. Degnan, T.W. Hussey, N.F. Roderick, and P.J. Turchi, IEEE Trans. Plasma Sci. **21**, 552 (1993).

²⁷ U. Shumlak, IEEE Trans. Plasma Sci., **23** 83 (1995).

²⁸ See National Technical Information Service Document No. DE94-011699 (J.D. Johnson, "SESAME Data Base"). Copies may be ordered from the National Technical Information Service, Springfield, Virginia 22161.

²⁹ D.E. Post, R.V. Jensen, C.B. Tarter, W.H. Grasberger, and W.A. Locke, Atomic Data and Nuclear Data **20**, 397 (1977).

³⁰ C.B. Tarter, J. Quant. Spectrosc. Radiat. Trans. **17**, 531 (1977).

³¹ H.W. Liepmann and A. Roshko, *Elements of Gasdynamics* (Wiley, New York, 1957).

³² IDL® Reference Guide (Research Systems, Inc., Boulder, CO, 1992).

³³ T.W. Hussey, in *Ultra High Magnetic Fields*, edited by V.M. Titov and G.A. Shvetsov (Nauka, Moscow, 1984) p. 208.

³⁴ S.M. Gol'berg and A.L. Velikovich, Phys. Fluids B **5**, 1164 (1993).

³⁵ D.L. Book, Phys. Plasmas **3**, 354 (1996).

³⁶ D.L. Youngs, Physica D **12**, 32 (1984).

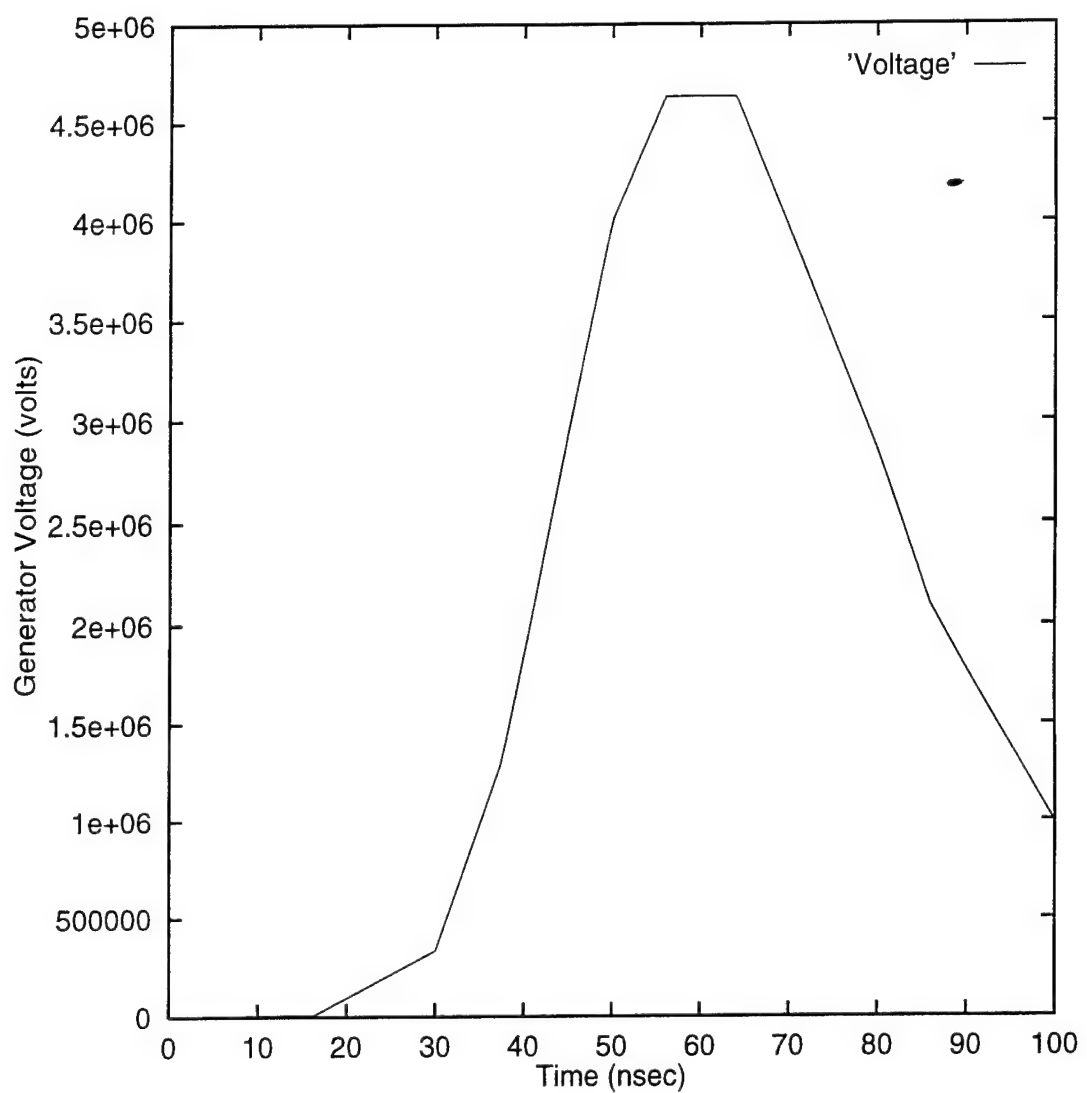


Figure 1. Numerical representation of Saturn voltage waveform.

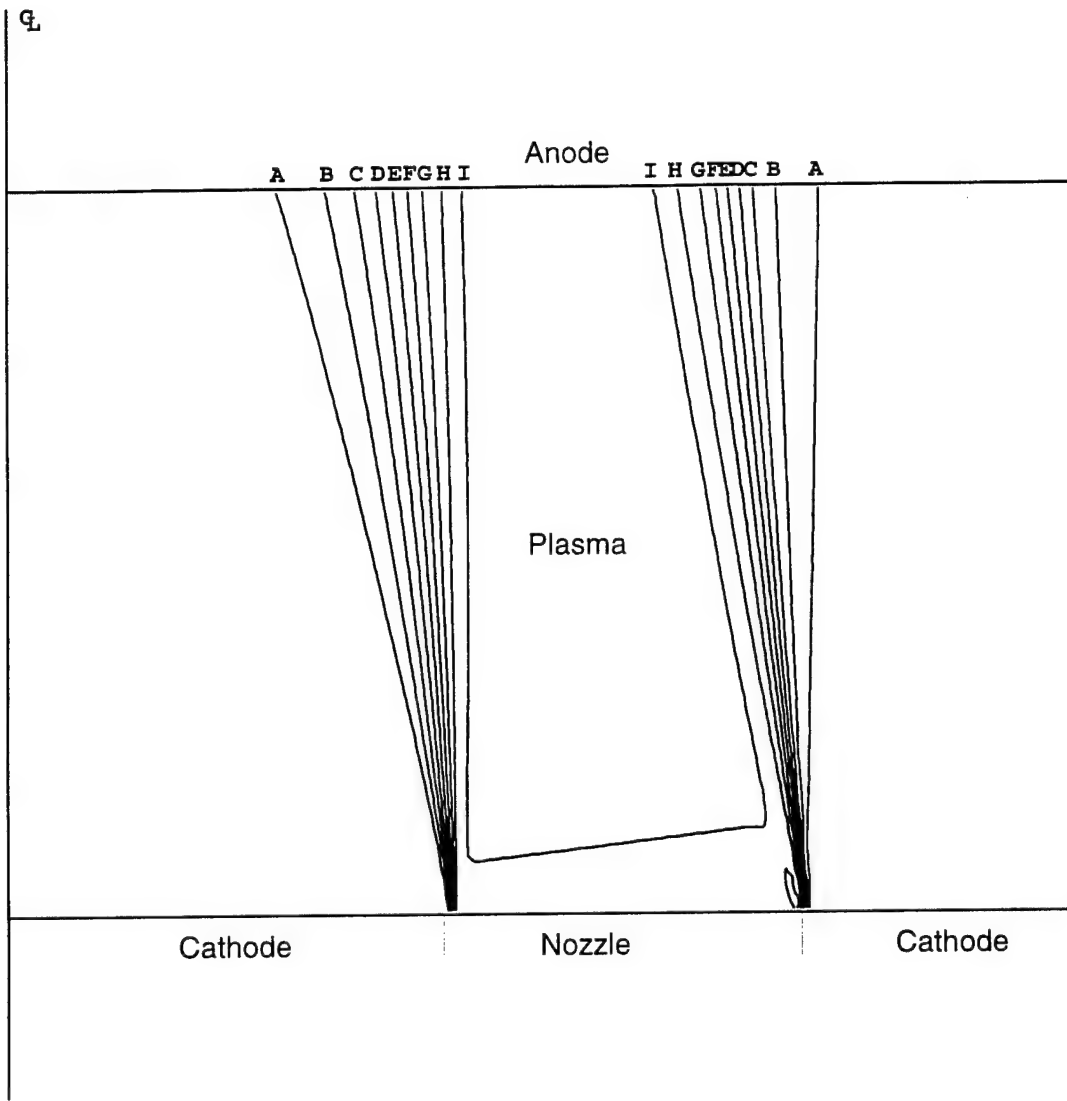


Figure 2a. Isodensity contours at $t = 0$; annular gas injection.

Contour levels (kg/m^3): $A=1.58 \times 10^{-3}$, $C=4.72 \times 10^{-3}$, $E=7.86 \times 10^{-3}$, $G=1.10 \times 10^{-2}$, $I=1.41 \times 10^{-2}$

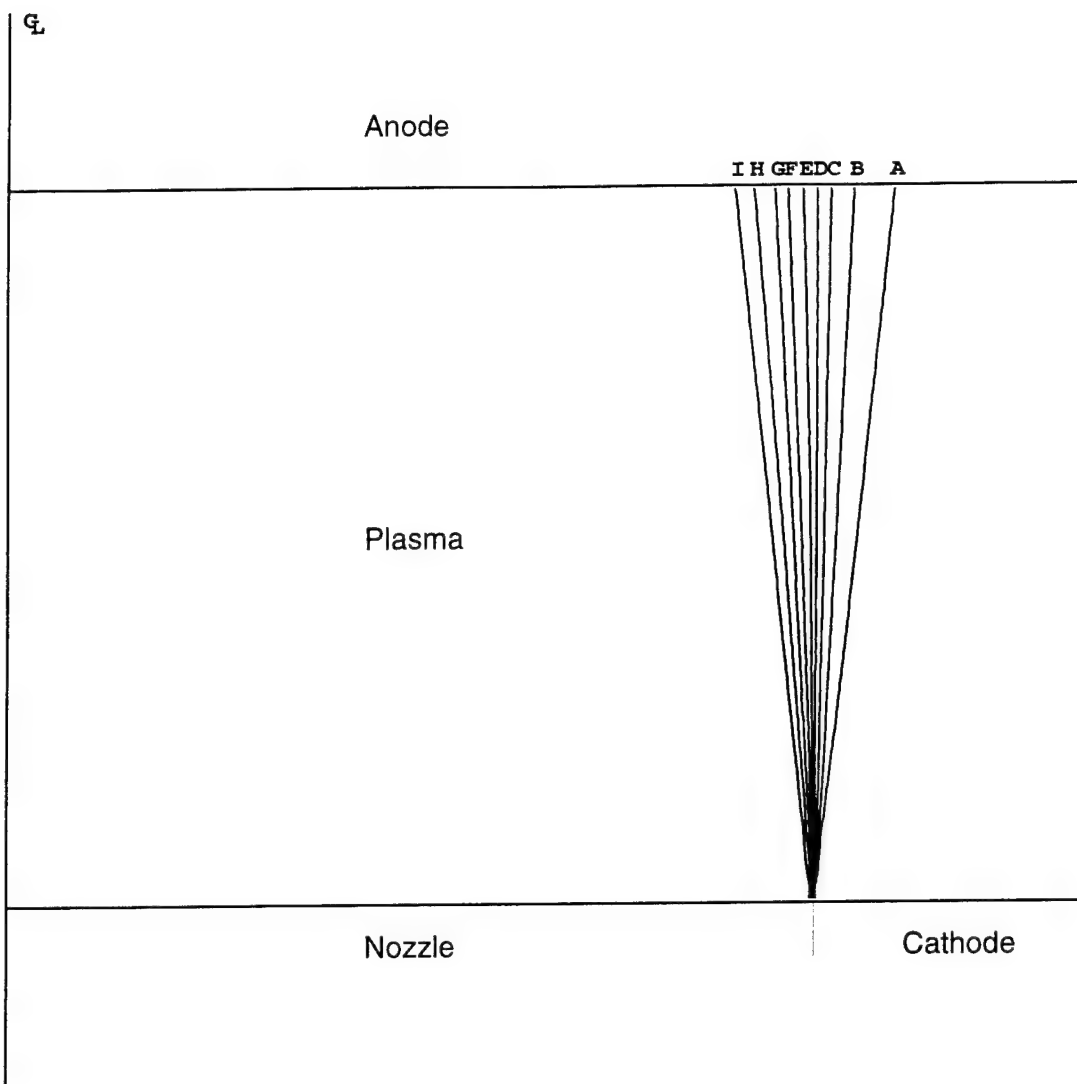


Figure 2b. Isodensity contours at $t = 0$; cylindrical gas injection.

Contour levels (kg/m^3): $A=1.57 \times 10^{-3}$, $C=4.88 \times 10^{-3}$, $E=7.81 \times 10^{-3}$, $G=1.09 \times 10^{-2}$, $I=1.40 \times 10^{-2}$

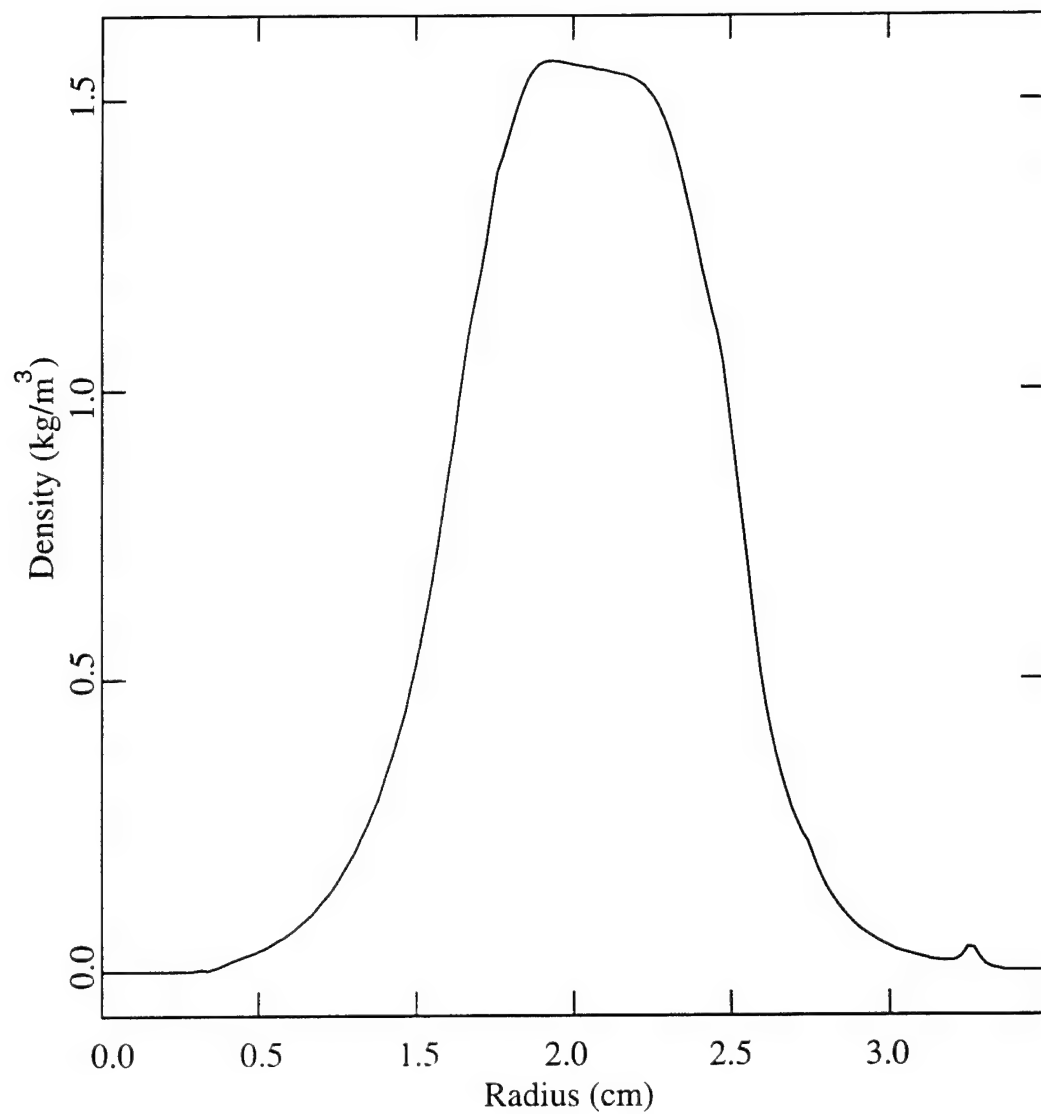


Figure 3a. Density vs. radius at top electrode at $t = 0$; annular gas injection.

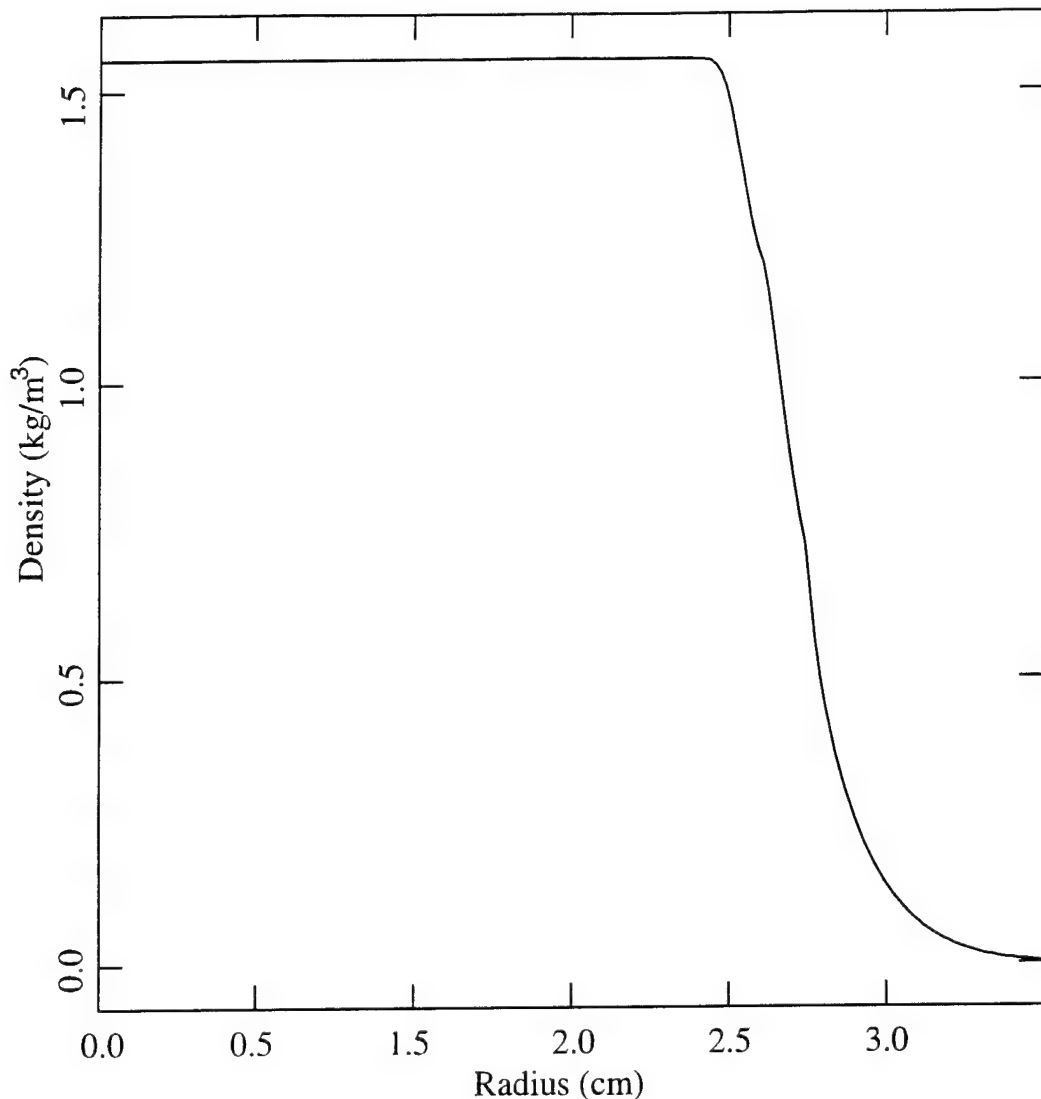


Figure 3b. Density vs. radius at top electrode at $t = 0$; cylindrical gas injection.

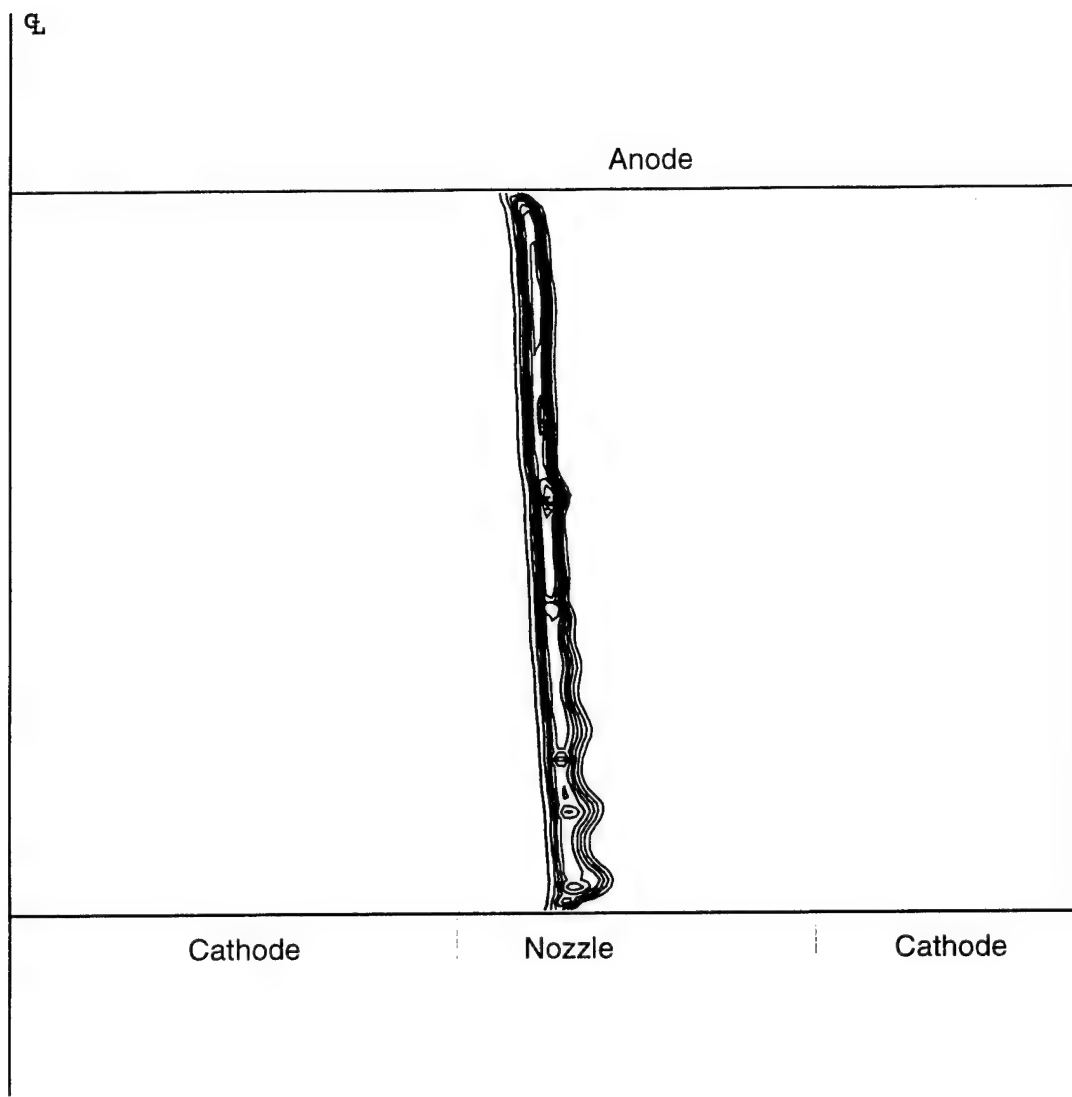


Figure 4a. Isodensity contours at $t = 70$ ns; annular gas injection.

Contour levels (kg/m^3): $A=2.18 \times 10^2$, $C=6.53 \times 10^{-2}$, $E=1.09 \times 10^{-1}$, $G=1.52 \times 10^{-1}$, $I=1.96 \times 10^{-1}$

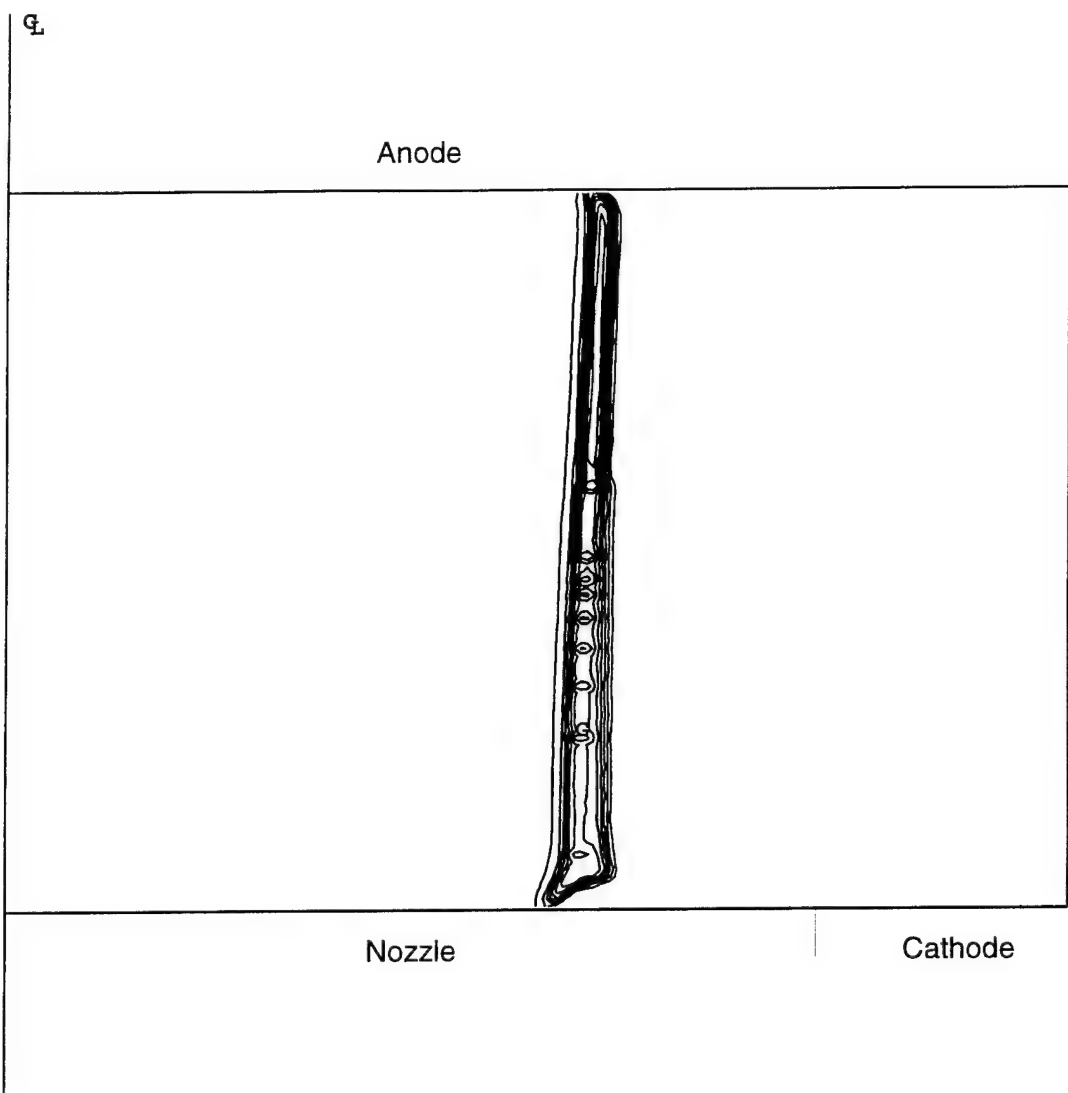


Figure 4b. Isodensity contours at $t = 70$ ns; cylindrical gas injection.

Contour levels (kg/m^3): $A=1.78 \times 10^{-2}$, $C=5.35 \times 10^{-2}$, $E=8.91 \times 10^{-2}$, $G=1.25 \times 10^{-1}$, $I=1.60 \times 10^{-1}$

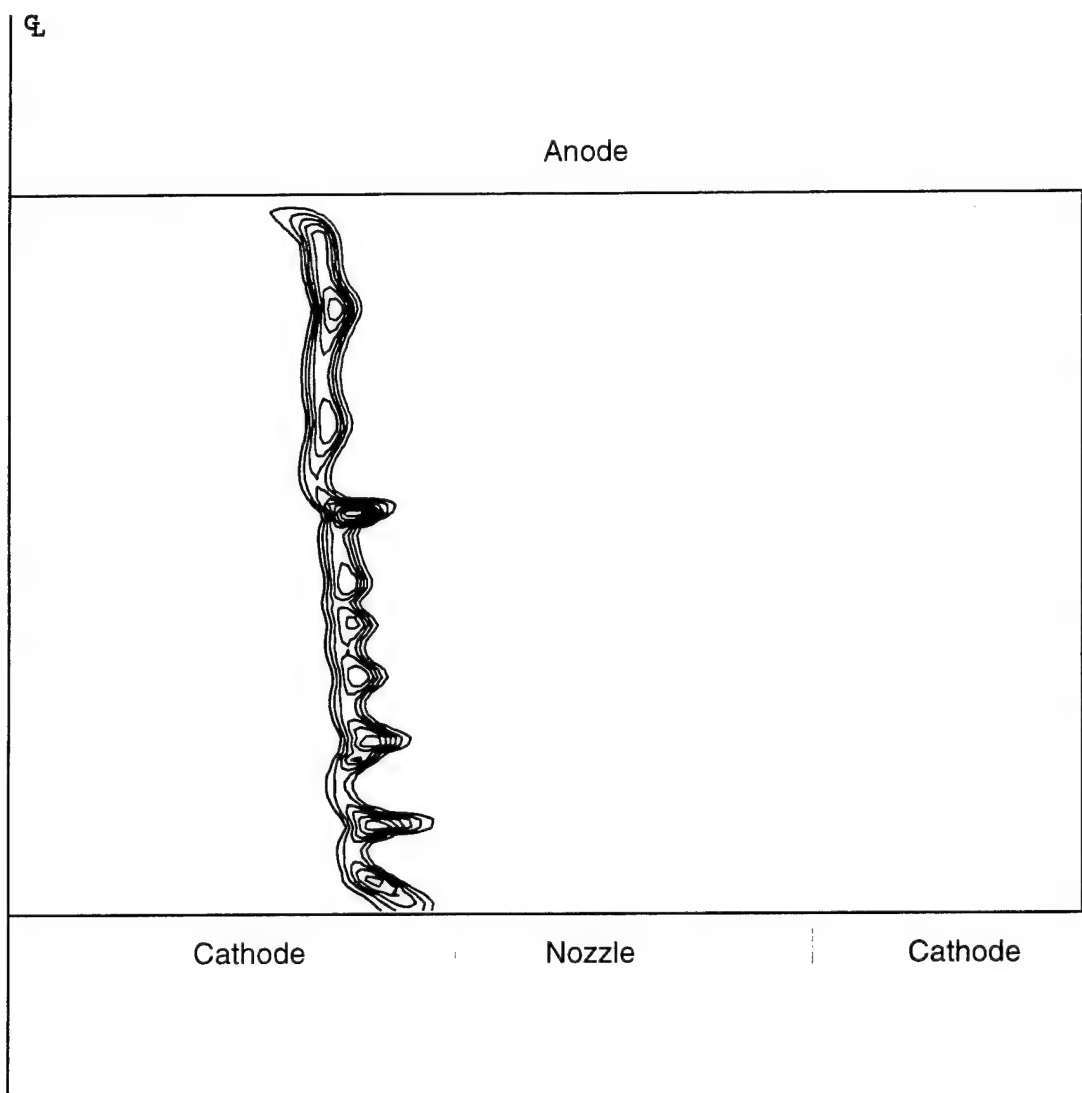


Figure 5a. Isodensity contours at $t = 80$ ns; annular gas injection.

Contour levels (kg/m^3): $A=5.47 \times 10^{-2}$, $C=1.64 \times 10^{-1}$, $E=2.74 \times 10^{-1}$, $G=3.83 \times 10^{-1}$, $I=4.92 \times 10^{-1}$

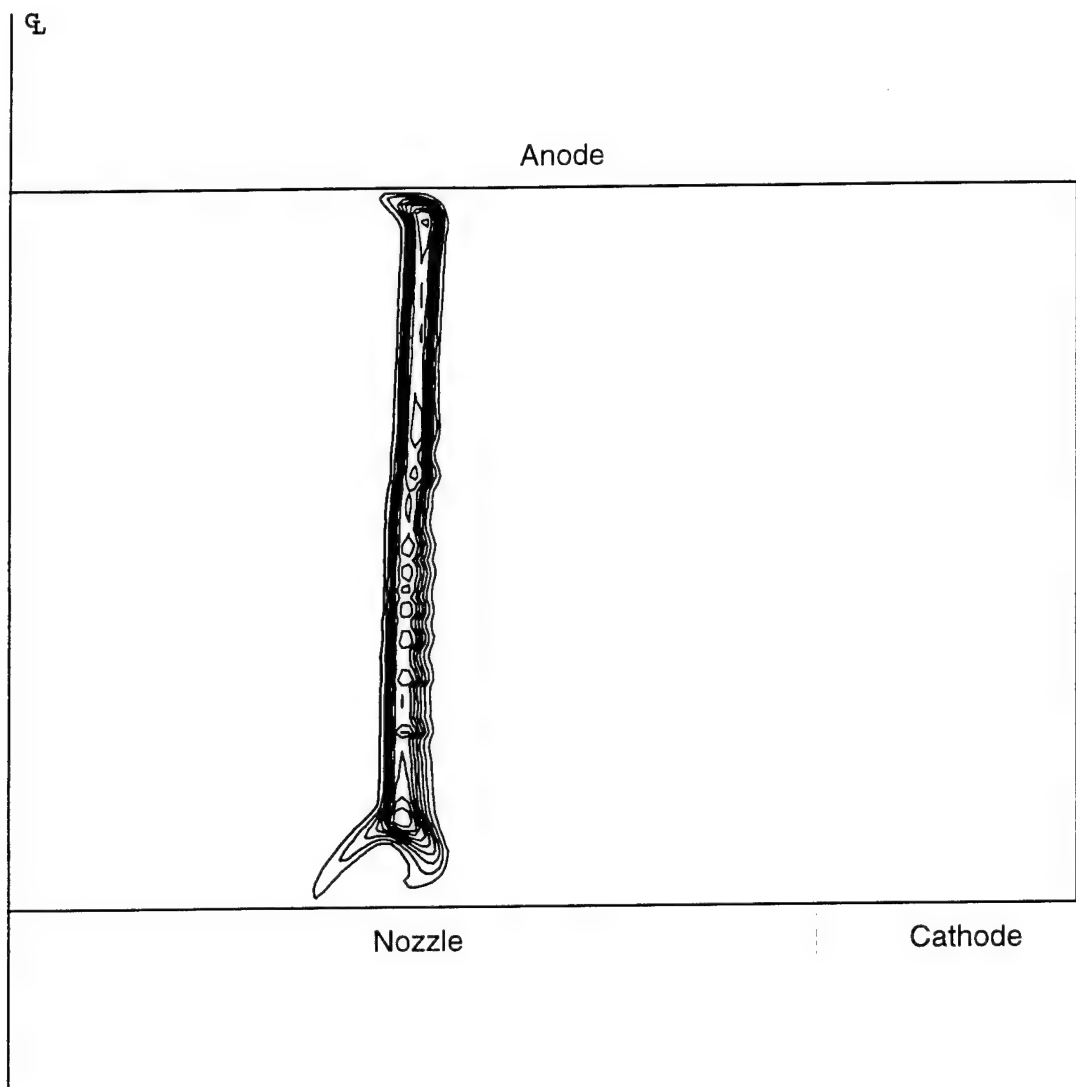


Figure 5b. Isodensity contours at $t = 80$ ns; cylindrical gas injection.

Contour levels (kg/m^3): $A=4.15 \times 10^{-2}$, $C=1.25 \times 10^{-1}$, $E=2.08 \times 10^{-1}$, $G=2.91 \times 10^{-1}$, $I=3.74 \times 10^{-1}$

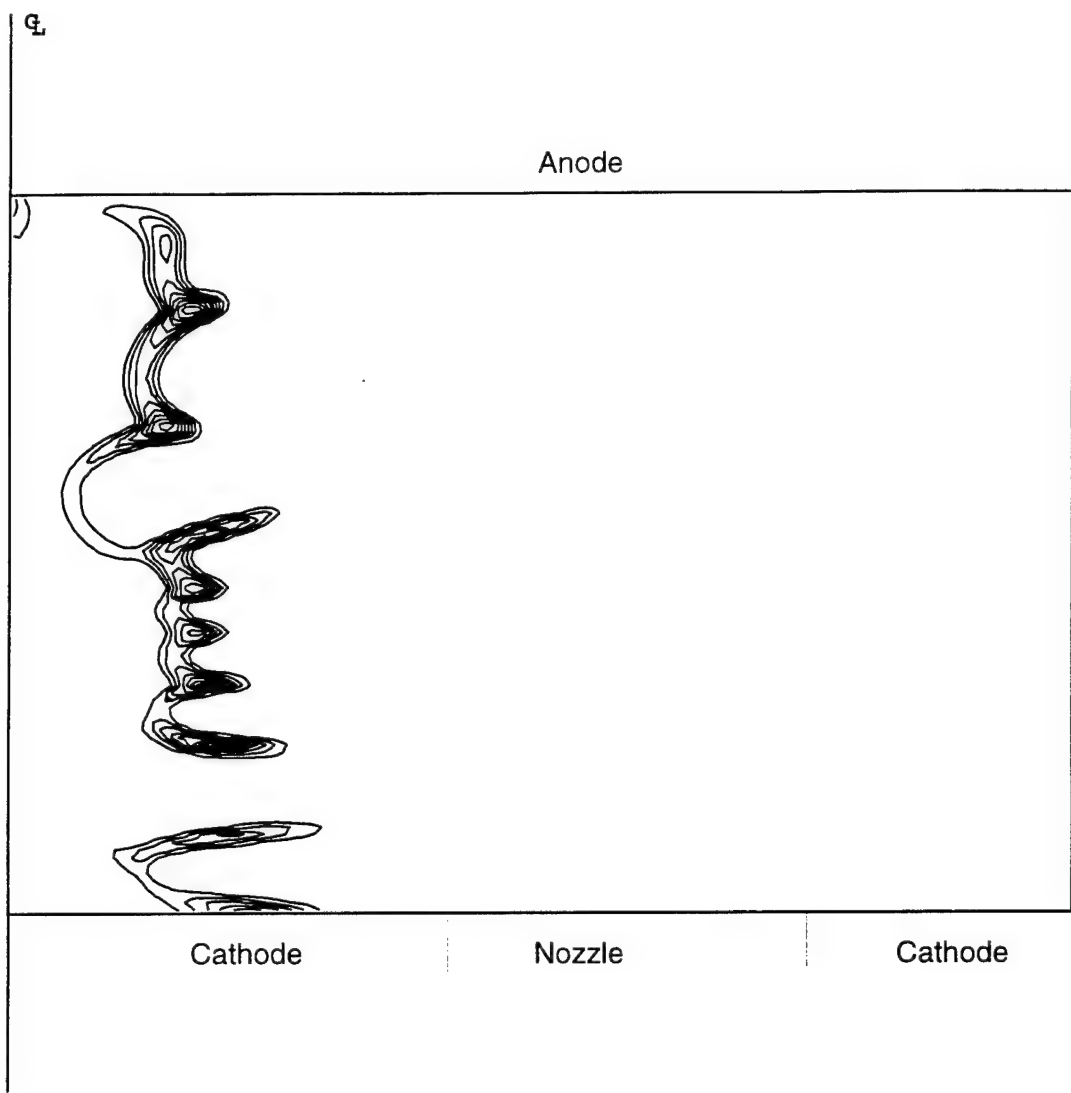


Figure 6a. Isodensity contours at 85 ns; annular gas injection.

Contour levels (kg/m^3): $A=1.06 \times 10^{-1}$, $C=3.17 \times 10^{-1}$, $E=5.28 \times 10^{-1}$, $G=7.40 \times 10^{-1}$, $I=9.51 \times 10^{-1}$

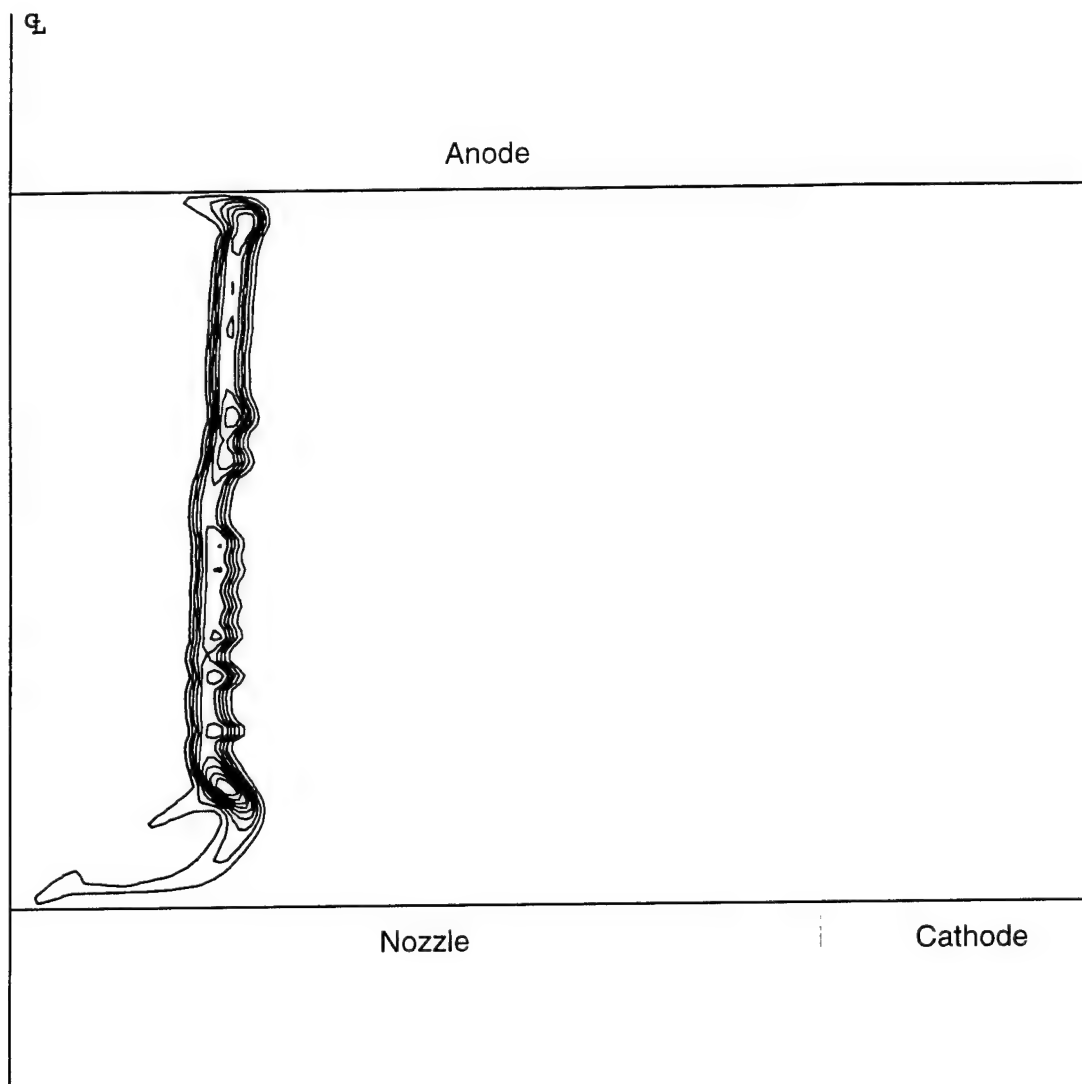


Figure 6b. Isodensity contours at $t = 88$ ns; cylindrical gas injection.

Contour levels (kg/m^3): $A=1.15 \times 10^{-1}$, $C=3.46 \times 10^{-1}$, $E=5.79 \times 10^{-1}$, $G=8.08 \times 10^{-1}$, $I=1.038$

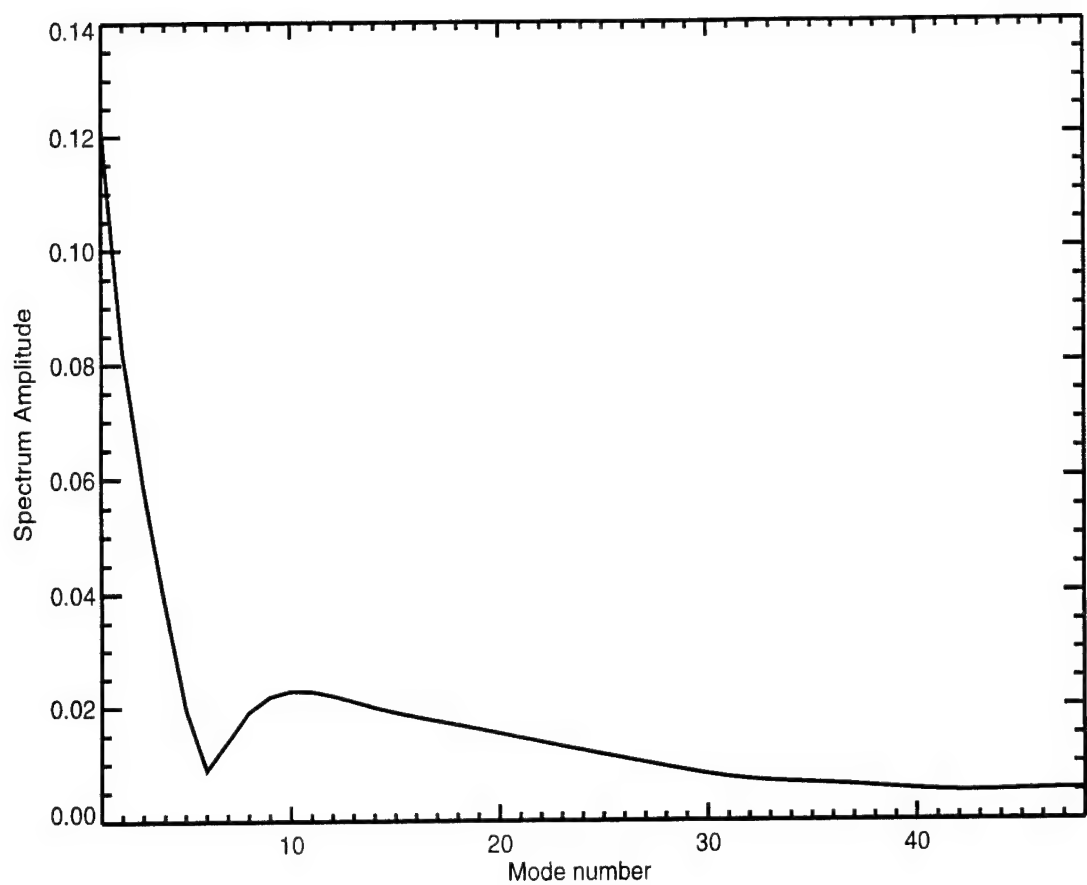


Figure 7a. Fourier spectrum of mass density at outer nozzle radius at $t = 0$; annular gas injection.

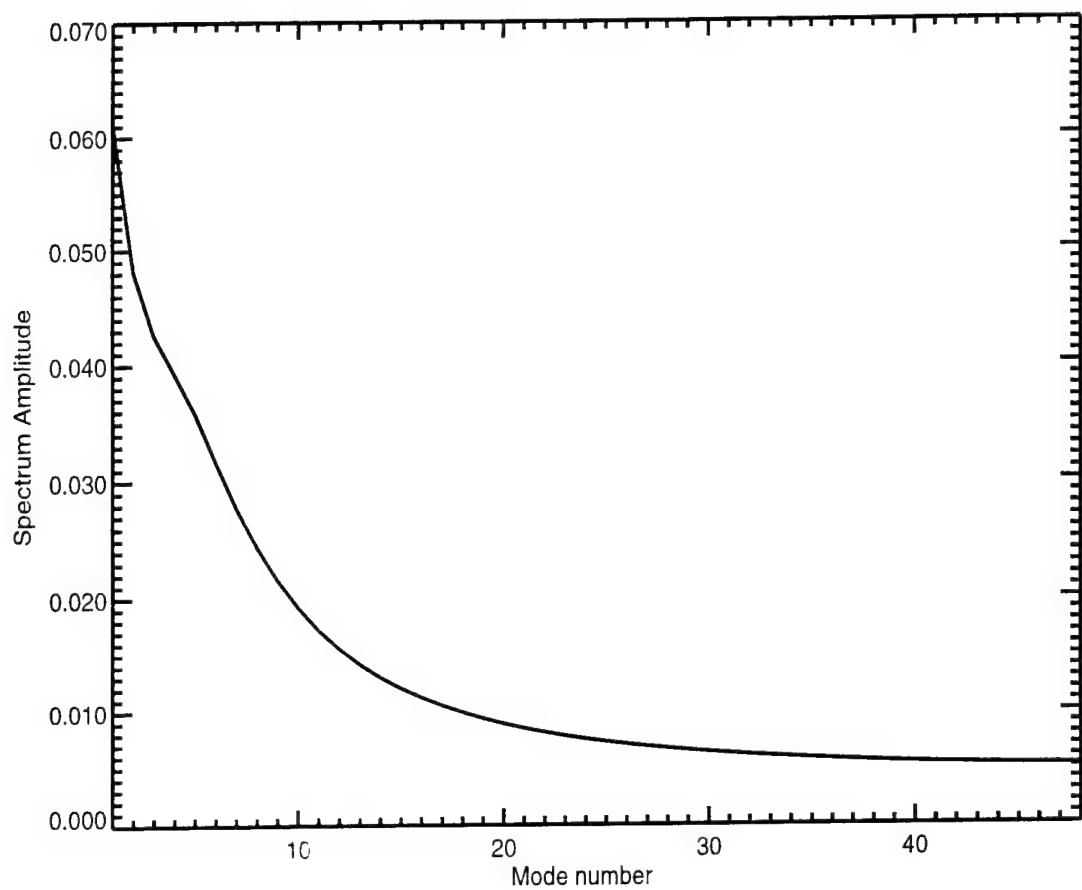


Figure 7b. Fourier spectrum of mass density at outer nozzle radius at $t = 0$; cylindrical gas injection.

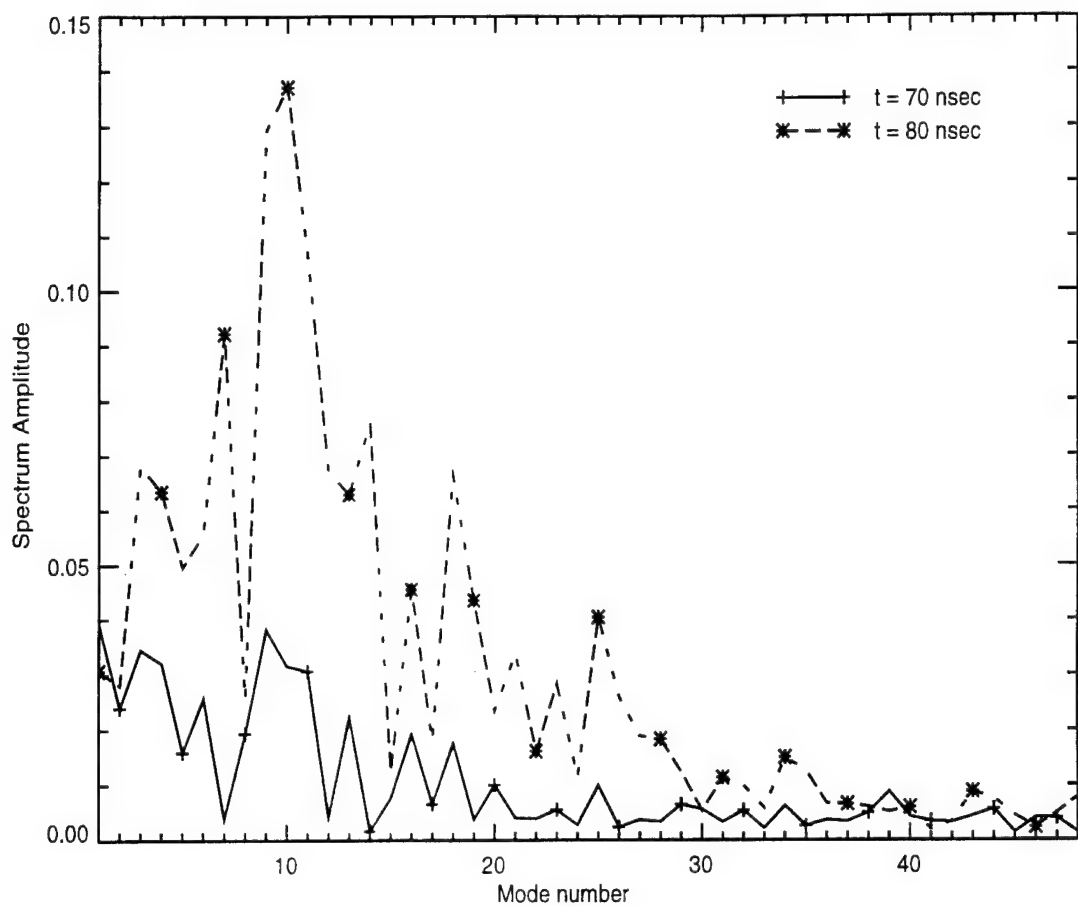


Figure 8. Fourier spectra of average mass density for annular injection at $t=70$ ns and $t=80$ ns.

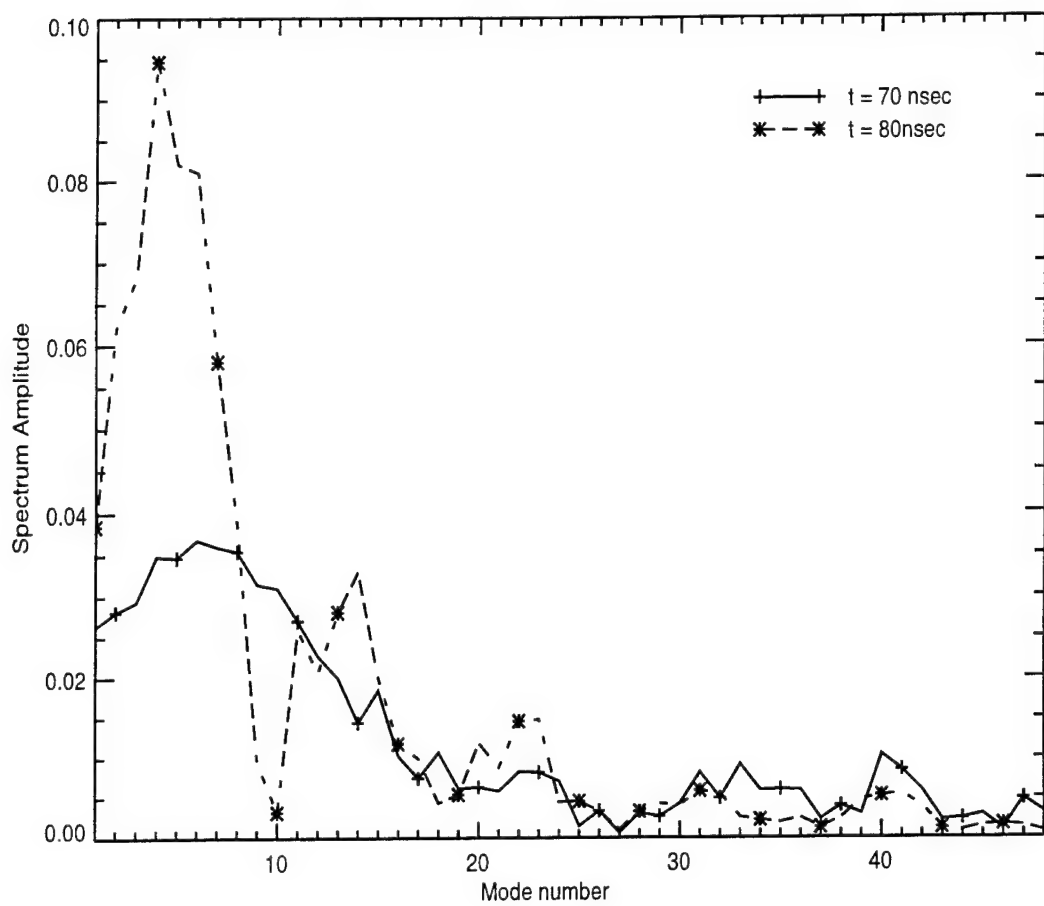


Figure 9. Fourier spectra of average mass density for cylindrical injection at $t=70$ ns and $t=80$ ns.

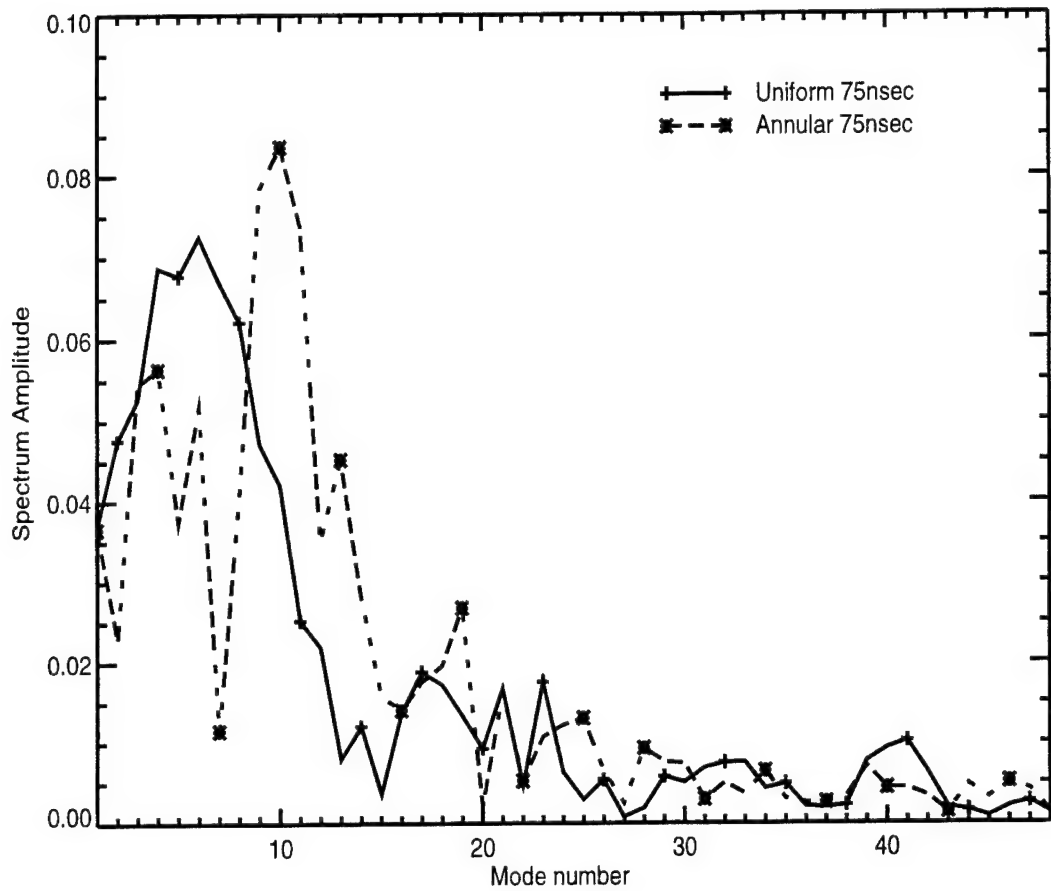


Figure 10. Fourier spectra of average mass density for annular injection and uniform injection when the plasma sheath is at approximately 1.25 cm radius.

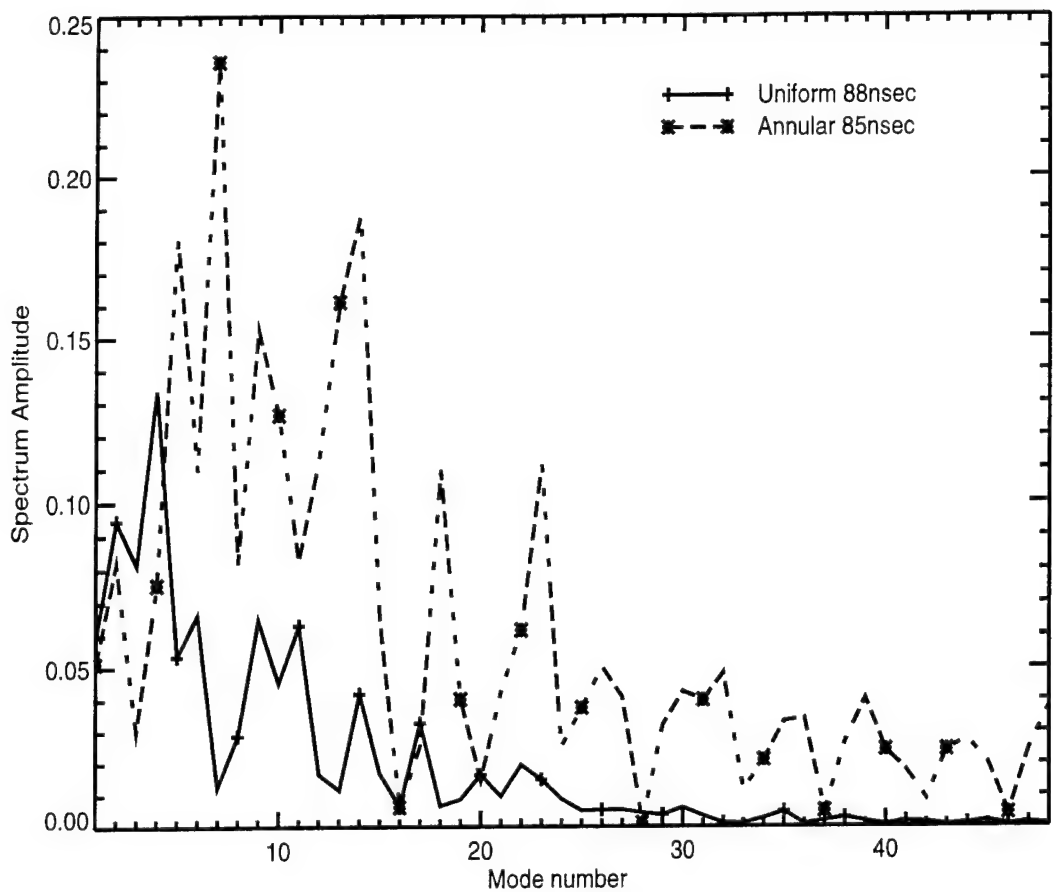


Figure 11. Fourier spectra of average mass density for annular injection and uniform injection when the plasma sheath is at approximately 0.50 cm radius.

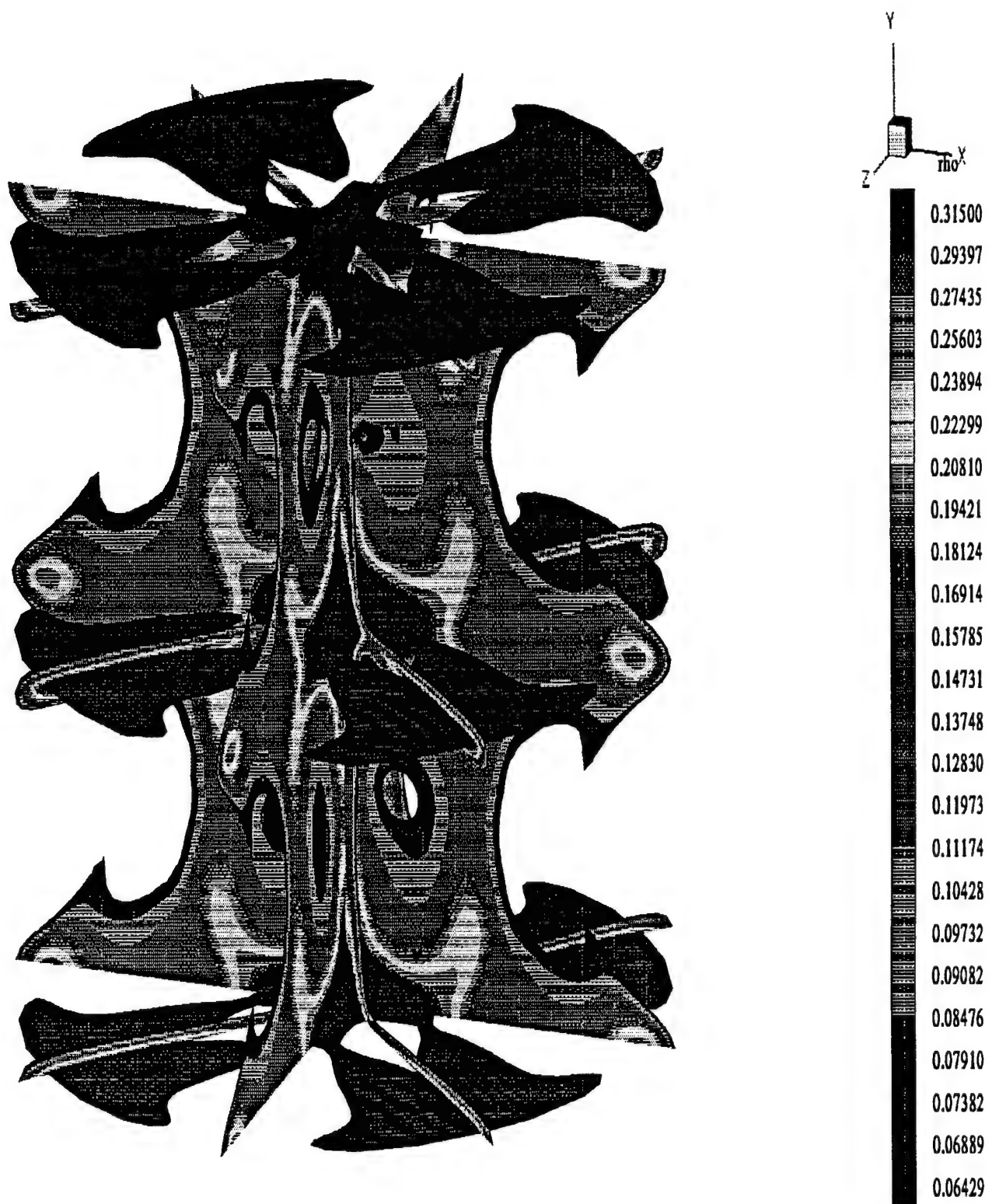


Figure 12. Mass isodensity plot, 8 cut planes and isodensity surface, at pinch for 20% perturbation.

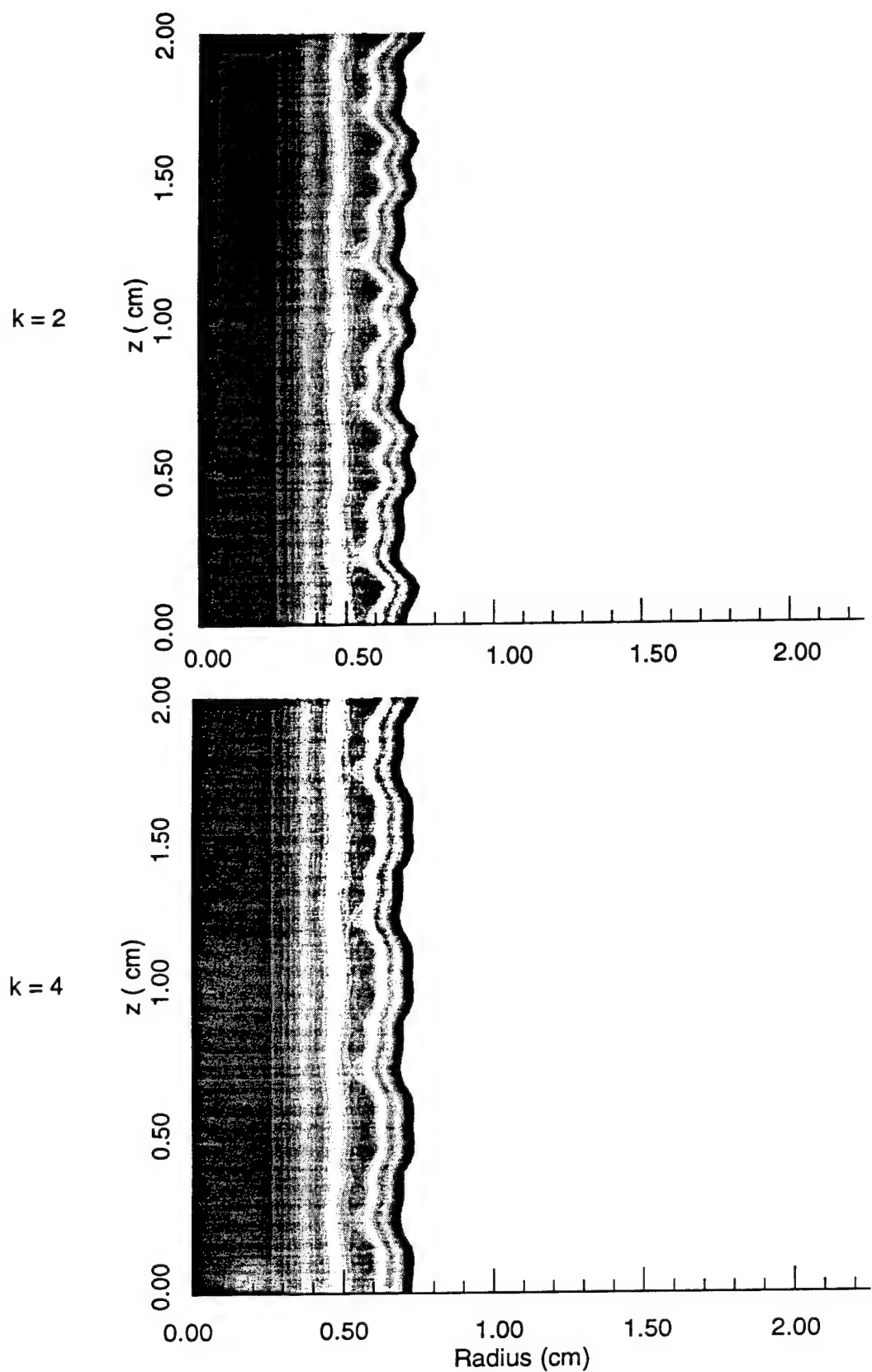
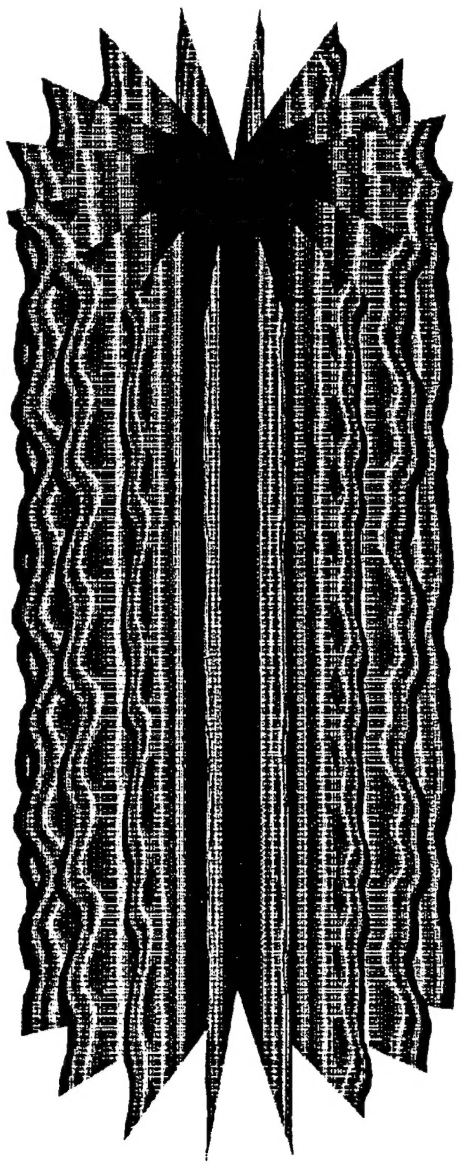
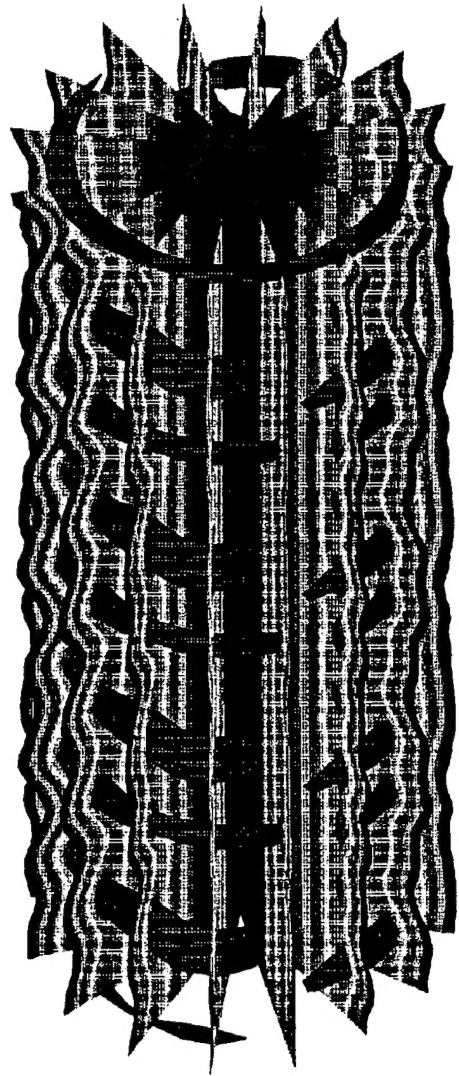


Figure 13. Mass isodensity plots for the $k = 2$ (top) and $k = 4$ (bottom) cut planes at $t = 62.5$ ns for the 5% random density perturbation.

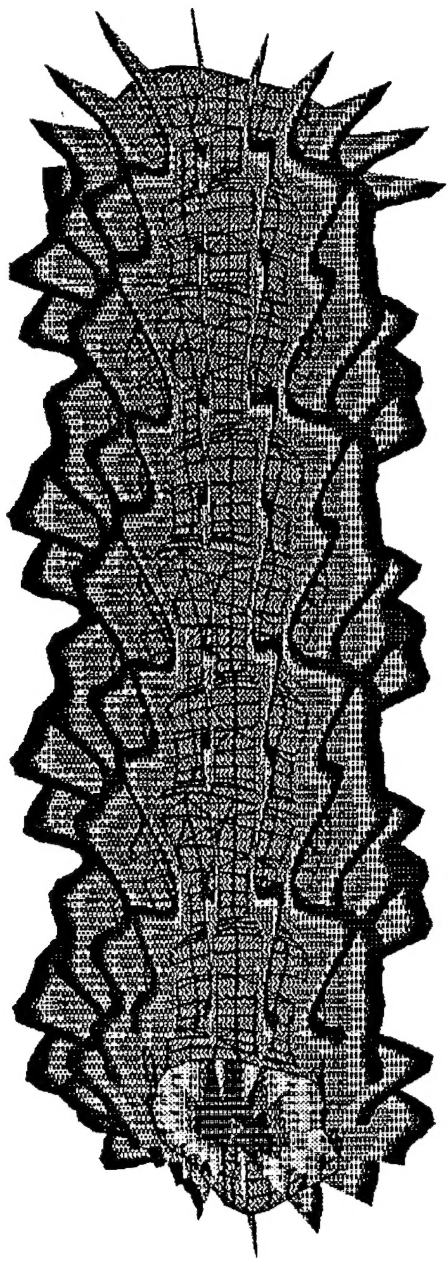


(a) 16 cut planes

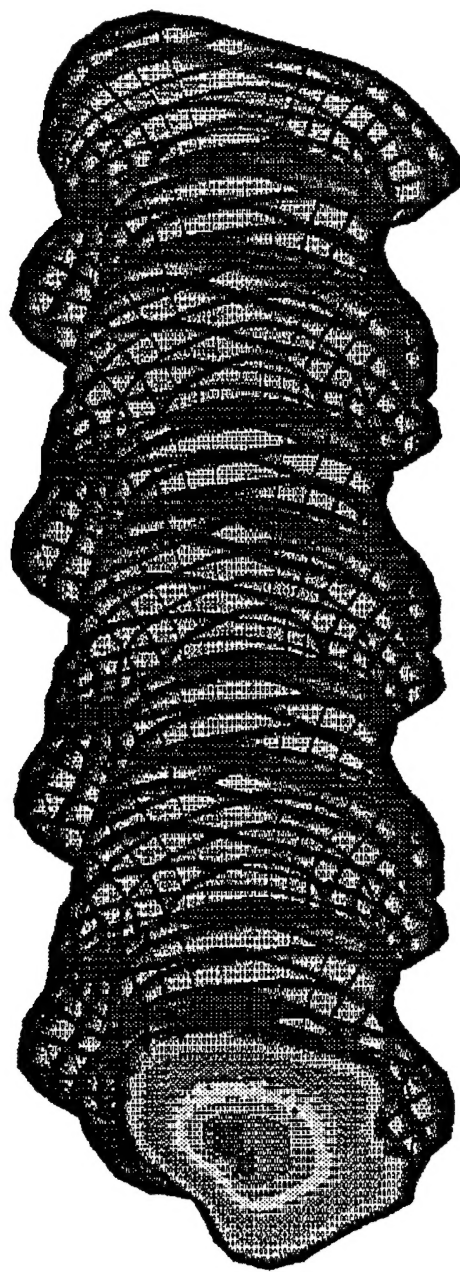


(b) 16 cut planes and isodensity surface

Figure 14. Mass isodensity plots near pinch $t = 62.5$ ns.



(a) Slice planes and isodensity surface



(b) Outer isodensity surface

Figure 15. Mass isodensity contours at pinch, $t = 67.5$ ns.

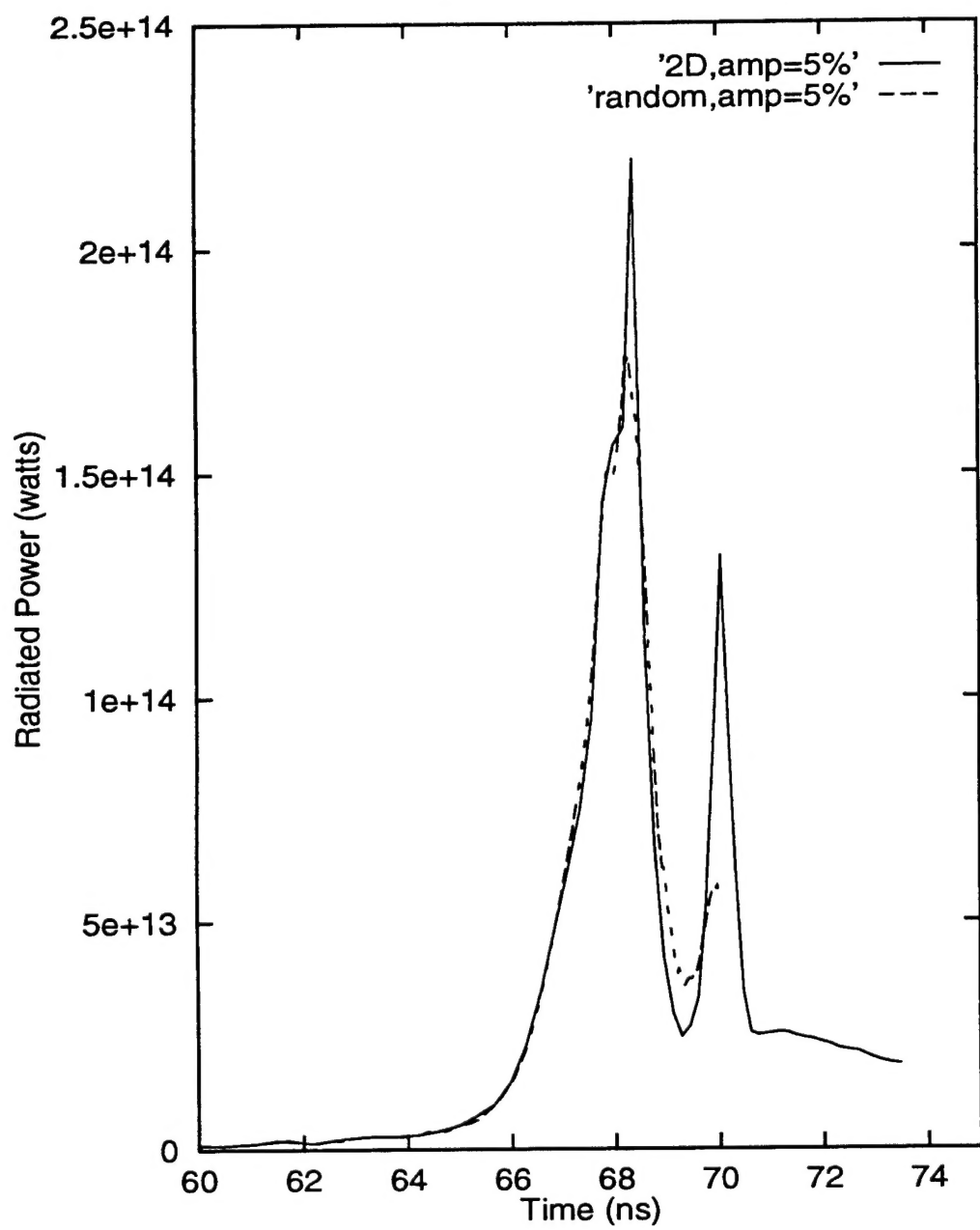


Figure 16. Radiated power vs. time for two-dimensional (solid line) and three-dimensional (dotted line) simulations with 5% random density perturbations.

Distribution List

AFSAA/SAI 1580 Air Force Pentagon Washington, DC 20330-1580	1 cy
AUL/LSE Bldg 1405 - 600 Chennault Circle Maxwell AFB, AL 36112-6424	1 cy
DTIC/OCP 8725 John J. Kingman Rd. Ste 0944 Ft. Belvoir, VA 22060-6218	2 cys
PL/HO 3550 Aberdeen Ave SE Kirtland AFB, NM 87117-5776	1 cy
PL/SUL 3550 Aberdeen Ave SE Kirtland AFB, NM 87117-5776	2 cys
PL/WSQ 3550 Aberdeen Ave SE Kirtland AFB, NM 87117-5776	10 cys